

Contactless Ground Penetrating Radar Imaging

*State of the art, challenges, and
microwave tomography-based data processing*



©SHUTTERSTOCK.COM/NULLPLUS

**ILARIA CATAPANO, GIANLUCA GENNARELLI, GIOVANNI LUDENO,
CARLO NOVIELLO, GIUSEPPE ESPOSITO, AND FRANCESCO SOLDOVIERI**

This article provides a comprehensive overview of the current state of the art in contactless ground-penetrating radar (GPR) systems. These devices offer many large-scale subsurface sensing possibilities based on different observation platforms and measurement configurations. On the other hand, new challenges must be faced because the radar system is not coupled directly to the ground; hence, data pro-

cessing plays a crucial role to achieve reliable imaging results. In this respect, microwave tomography (MWT) turns out to be a very flexible tool to address the aforementioned challenges. This methodology allows modeling, in a relatively simple way, of the radar signal propagation in an inhomogeneous medium as well as the handling of arbitrary measurement modalities and radar configurations. Experimental examples regarding different types of contactless GPR are presented to validate the effectiveness of MWT when combined with ad hoc signal filtering procedures.

Digital Object Identifier 10.1109/MGRS.2021.3082170
Date of current version: 15 June 2021

GPR GENERAL CONCEPTS

GPR is designed to detect and localize buried or hidden targets by exploiting the ability of electromagnetic (EM) waves, mainly radio-frequency and microwave signals, to penetrate nonmetallic media such as subsoil and construction materials [1]. The GPR working principle is simple: a transmitting (Tx) antenna radiates an incident field that impinges on a target (buried or embedded), and consequently, the target backscatters a field that is collected by a receiving (Rx) antenna.

The backscattered field conveys information about the EM properties and geometry of the target. This information can be uncovered from the measured signal via dedicated data processing and modeling techniques [1]–[3].

GPR is widely used for nondestructive inspections in a large number of civil and noncivil applications. Some examples include

- geophysics, where GPR is used for ice analysis [4], soil stratigraphy characterization [5], water table localization [6], water content definition [7], and mining activities [8]
- archeology, where GPR is an assessed tool used to map ruins and address excavations [9], [10]
- structural inspections and damage assessment for safety and security purposes [11], [12]
- forensic surveys [13], demining [14], anthropic risk mitigation [15], and planetary investigations [16].

These use cases give an idea of GPR's wide applicability and explain the huge attention that this technology has received through the years since its first documented application [17]. Starting from the second half of the 19th century, a rich literature has been produced, reporting on hardware design, data processing, and measurement campaigns [1]. However, despite its simple sensing principle, GPR data processing is a not trivial task and involves two main challenges, which affect the reliability and accuracy of its results. The first issue is the extraction of the field backscattered by the target from the collected data, which requires proper noise and clutter-filtering procedures [1]–[3]. The second one is the reconstruction of the EM target features, which involves the solution of a nonlinear and ill-posed inverse scattering problem [18].

GPR can be operated under different measurement configurations [1]–[3]. The most popular arrangement is the multibistatic one, where a Tx and an Rx antenna with a common spatial offset move together along a line to collect the backscattered field. When a single antenna operates simultaneously as transmitter and receiver (zero offset) or when the distance between the Tx and Rx antennas is small in terms of the radiated wavelength, the configuration is known as *multimonostatic*. Common midpoint is another popular configuration [1], where the Tx and Rx antennas progressively move away from one another with a fixed midpoint between them. This configuration is mainly exploited to estimate the EM properties of the background, i.e., the medium where the targets

are located. Finally, multioffset or multistatic configurations [2], which allow data collection at several points for a single transmitter's position, have been proposed not only to estimate the EM properties of the background but also to achieve improved imaging of the buried scenario. However, at the current development state of GPR technology, this last configuration is impractical for large-scale surveys. In addition, by restricting the attention to qualitative GPR imaging, the achievable improvements in terms of resolution are not significant because the additional information provided by spatial diversity is not completely independent from that achieved by the frequency diversity [2].

This article provides an overview of GPR systems and data processing in contactless scenarios, i.e., a GPR antenna at least a few wavelengths from the investigated region. Such a remote sensing configuration is different from the one usually adopted for GPR surveys, where the antenna is in contact with the probed medium. Moreover, we consider GPR on several observational platforms, such as satellites, aircrafts, drones, terrestrial vehicles, and working in down-looking (DL-GPR) and forward-looking (FL-GPR) modes. In detail, the article aims at reviewing contactless GPR systems and their main applications as well as to provide a detailed description of the issues to be faced and of the relevant data processing/inversion approaches.

STATE OF THE ART: APPLICATIONS AND SYSTEMS

The necessity of investigating wide areas and improving the efficiency of fieldwork motivates the design and setup of fast GPR measurement configurations. GPR systems are most often mounted on-board vehicles in several application fields, such as archaeological prospections [9], [10], road and railway quality assessment [19], [20], civil engineering [12], landmines and unexploded ordnances (UXOs) detection [14], and so on. Within that context, GPR may operate in both air- and ground-coupled configurations. Air-coupled systems are often preferred as they allow for recording data at a much higher rate without damaging the antennas [21]. As reported in [22], the antennas can be considered air-coupled when it is possible to resolve the surface reflection event from the direct pulse. However, using air-coupled antennas decreases the performance of GPR, mainly in the presence of water-saturated media, because only a limited portion of the impinging signal is transmitted into the ground.

The air-coupled configuration allows for GPR data collection in two different modalities, i.e., in the DL-GPR and FL-GPR modes. The next sections present several examples of air-coupled GPR systems installed on ground and aerial (including drone and satellite) platforms. Table 1 summarizes the main characteristics of most of the radar systems discussed in the "State of the Art: Applications and Systems" section based on the available literature data.

DL-GPR ON GROUND VEHICLES

Contactless DL-GPR systems are generally mounted on a holding bracket attached to the front or rear bumper of a vehicle and suspended in the air at a height above the ground variable in the range of 0.15–0.5 m [19]. The elevated antenna configuration reduces both the antenna-ground coupling and the antenna-target interactions, thus reducing the

overall clutter. Nonetheless, part of the signal is reflected back from the ground, consequently reducing the penetration depth [1]. Both the time-domain and stepped-frequency continuous-wave (SFCW) architectures are operated in DL mode [1], [2].

DL-GPR is extensively applied for road-quality assessment [19], [23]–[27]. For this application, GPR is typically

TABLE 1. THE MAIN FEATURES OF THE CONTACTLESS GPR SYSTEMS DESCRIBED IN THE “STATE OF THE ART: APPLICATIONS AND SYSTEMS” SECTION.

REFERENCE	APPLICATION	MODEL/ANTENNA	TECHNOLOGY	CENTER FREQUENCY/ BANDWIDTH (MHz)	PENETRATION DEPTH
[20]	Railways inspection	MALÅ 800	Pulsed	800	<1 m
[24]	Road inspection	GSSI Model H4205	Pulsed	1,200	<1 m
[26]	Road inspection	Horn antenna	Pulsed	1,000	<1 m
[27]	Road inspection	3D-Radar V1821	SFCW	200–3,000	<1 m
[28]	Railways inspection	GSSI SIR-10A	Pulsed	900	<1 m
[31]	Railways inspection	RIS- Hi Pave	Pulsed	1,000, 2,000	<1 m
[32]	Railways inspection	Multichannel GPR	Pulsed	300	<2 m
[38]	Landmines and UXO detection	Stanford Research Institute	SFCW	500–3,000	Not specified
[40]	Landmines and UXO detection	Planning Systems Corporation	SFCW	400–4,000	Not specified
[41]	Landmines and UXOs detection	SIRE	Pulsed	300–3,000	Not specified
[42]	Landmines and UXOs detection	Lawrence Livermore National Laboratory multistatic GPR	Pulsed	300–1,800	<0.2 m
[49]	Ice exploration	TUD radar	Pulsed	60	<3.37 km
[50]	Ice exploration	ICARDS	Pulsed	150	<3 km
[51]	Ice exploration	MCORDS/I	Pulsed	195	<4 km
[52]	Ice exploration	MCORDS/I accumulation radar	Pulsed	590–910	<500 m
[52]	Ice exploration	MCORDS/I Snow radar	Pulsed	5,000	<40 m
[54]	Ice exploration	RST GmbH radar	Gated SFCW	50–150	<300 m
[61]	Detection of aquifers in arid areas	OASIS	Pulsed	50	<4 km
[62]	Ice and desert exploration	CO.RI.S.T.A	Pulsed	145–185	<100 m
[65]	Under-foilage imaging	CARABAS	Pulsed	20–90	Not specified
[66], [67]	Planetary exploration	SHARAD	Pulsed	15–25	<1,500
[68], [70]	Planetary exploration	MARSIS	Pulsed	1–5	A few kilometers
[69]	Planetary exploration	SELENE	Pulsed	5	A few kilometers
[71]	Environment monitoring	Linear array	Pulsed	100	None
[72]	Environment monitoring	Linear array	FMCW	—	None
[73]	Ice monitoring	Patch array	FMCW	80–200 (variable)	A few meters
[74]	Forest mapping	Log periodic	Pulsed	250–350	None
[74]	Environmental monitoring	Horn array	Pulsed	9,400–9,800	None
[75]	Environment monitoring	Patch array	FMCW	5,275–5,325	None
[75]	Environment monitoring	Patch array	FMCW	9,600–9,700	None
[76]	Landmines and UXOs detection	Horn antenna	SFCW	350	A few centimeters
[76]	Security and Earth observation	Helix antennas	Pulsed	2,200	None
[78]	Archaeology and geology	LPDA antennas	FMCW	510	<20 m
[79]	Landmines and UXOs detection	Vivaldi antipodal antenna	Pulsed	56	<0.2 m
[80]	Archaeology/infrastructure monitoring	LPDA antennas	Pulsed	3,100–4,800	Not specified
[81]	Landmines and UXOs detection	Horn antennas	FMCW	1,000	Not specified
[82]	Snow/ice monitoring	Vivaldi antennas	Pulsed	5,000	A few meters
[83]	Soil moisture mapping	Hybrid horn-dipole antenna	Pulsed	250–2,800 (variable)	Not specified
[84]	IEDs detection	Ultrahigh-frequency-ultrawide-band radar	FMCW	500–3,000 (variable)	Not specified
[85]	Landmines/UXOs detection	Helix antennas	Pulsed	3,100–4,800	<1.5 m

MCORDS/I: multichannel radar sounder/imager.

equipped with horn antennas and mounted on a car or van for high-resolution diagnostics of the shallower road layers. In [26], two 2-GHz, air-coupled, bistatic GPR systems were used to estimate the dielectric constant of the pavement surface. In [27], the GeoScope step-frequency array system, manufactured using 3D radar and covering a 200–3,000-MHz bandwidth, was employed; such a system enabled measurements using 21 antenna pairs by providing coverage of a 1.5-m wide area with a line spacing of 75 mm in the transverse direction.

Air-coupled DL-GPR is likewise installed on-board trains to quickly and efficiently assess the status of railways over long distances and of tunnel structural conditions [28]–[32]. Most of the studies in this field are focused on the development of methods for evaluating the conditions of ballasted railway track beds, and an exemplary study based on a 900-MHz antenna is reported in [28]. More recently, high-frequency air-coupled systems operating at central frequencies of 1 and 2 GHz were tested [20], [30], [31] due to their advantages in terms of simplicity of use and improved resolution.

FL-GPR ON GROUND VEHICLES

Contactless FL-GPR systems, such as for landmines and UXOs detection, have been developed primarily for military operations [33]–[37]. In FL-GPR sensing, the image area is always ahead of the radar platform at a safe-enough distance to guarantee the security of the operators involved in the survey. FL-GPR systems are mounted in front of a vehicle, and the data can be gathered under synthetic, real, and virtual aperture configurations [34]. The FL-GPR with a synthetic aperture takes advantage of an antenna moving along a track [33] to form the aperture. The FL-GPR with a real aperture uses a physical array, with each element being a transceiver [38]. The virtual aperture can be obtained by means of a multiple-input, multiple-output (MIMO) array made by M transmitters and N receivers ($M \times N$ virtual transceivers). In this way, it is possible to reduce the system complexity with respect to the architectures based on physical arrays [34], [35], [39].

A FL-GPR was developed by Planning Systems Corporation [40]. The system generates a SFCW signal in the range of 400 MHz–4 GHz and performs digital phase detection of continuous-wave echoes on a fixed number of Rx antennas. The Stanford Research Institute developed a stepped-frequency FL-GPR prototype working in the frequency range of 500 MHz–3 GHz [38]. The synchronous impulse reconstruction radar is an ultrawideband pulsed radar with a 300-MHz to 3-GHz bandwidth developed at the U.S. Army Research Laboratory [41]. A multistatic GPR system consisting of 16 transmitter and receiver pairs mounted across the front of a vehicle and capable of real-time imaging and object detection was developed at the Lawrence Livermore National Laboratory [42].

An undesired effect encountered in FL-GPR imaging is the reduced-wave coupling in the soil due to the adopted

data-acquisition geometry. Furthermore, surface roughness and subsurface clutter may have a strong impact on the imaging performance. For these reasons, computational EM tools based on advanced scattering models were developed to predict radar performance under various environmental clutter conditions [37]. A real-time 3D modeling of moving-platform FL-GPR scattering from rough terrain was reported in [43]. MWT approaches for FL-GPR imaging were developed in [35]. Specifically, in [35], the imaging performances of the beamforming and MWT approaches were analyzed and compared under flat and rough terrain conditions. Likelihood-ratio test-based detectors were considered in [44] and [45] to detect landmines and low-signature targets, while coherence-factor-based rough-surface-clutter suppression was recently reported in [46].

AIRBORNE AND SATELLITE-BASED GPRs

A remarkable class of contactless GPRs includes airborne penetrating radars or sounders [47]–[65]. These systems are valuable in many application fields, such as geophysics, environmental monitoring, security, archeology, and so on. Airborne GPRs enable the inspection of wide geographical areas, sometimes inaccessible or hostile (glaciers, deserts, and so forth), by quickly collecting a large amount of data.

Airborne sounders were originally developed for glacier exploration and operated at frequencies ranging from some megahertz to a few gigahertz (for example, see [51] and [52]). As is well known, ice is a very favorable environment for radar signal propagation due to its low EM losses [1]. Based on the operating frequency and ice conditions (temperate, cold, and so on), sounders can reach high penetration depths of up to few kilometers [49], [53]. The first study on the topic [47] revealed the capability of detecting the thickness of radio-transparent stratified materials by means of EM pulses at the very-high-frequency (VHF) range. A survey carried out in 1964 over the northwest Greenland ice sheet using an airborne sounder provided the first ice thickness profile [48]. The surface and bottom topography of the central Greenland ice sheet were later determined using the Technical University of Denmark (TUD) radar, which is a 60-MHz ice sounder [49].

In 1998, researchers at Kansas University developed the 150-MHz Improved Coherent Arctic Radar Depth Sounder (ICARDS) system for exploring glaciers [50]. Over the years, researchers have enhanced the system, developing a pulsed multichannel radar sounder/imager that is designed to estimate the bedrock and determine the inner glaciers' stratigraphy [51], [52]. The system operates at the central frequency of 195 MHz, with a 30-MHz bandwidth and variable peak power of up to 1,200 W. The experimental tests carried out in Antarctica and Greenland demonstrated the ability to reach penetration depths of up to 4 km. The other penetrating radars for ice investigations are presented in [52]. The first one, known as *accumulation radar*, operates close to the L band (590–910-MHz band), which is suitable

for the exploration of shallow glaciers (depths <500 m). The second radar, called *snow radar*, works at higher frequencies (a center frequency of 5 GHz, with a band of up to 6 GHz) to measure the thickness of the snow layer on ice (depths <40 m). The use of a Ku-band radar was also proposed to evaluate the ice-surface topography and shallower internal layering (depths <10 m) [52]. Further airborne sounders for ice exploration were reported in [53]–[60].

As a part of the OASIS project funded by NASA, a 50-MHz airborne GPR was designed to estimate ice thickness and detect aquifers in arid areas. An experiment conducted over the Kuwait desert in 2011 proved the capability of detecting a water table at a depth of approximately 50 m [61]. A VHF airborne sounder, with a bandwidth of 145–185 MHz, was developed by the research consortium Consorzio di Ricerca su Sistemi di Telesensori Avanzati (CO.RI.S.T.A.) in the framework of a research project funded by Italian Space Agency [62].

Airborne GPRs have attracted considerable attention for subsurface target detection and under-foliage imaging applications [63], [64]. A popular example in this field is the Coherent all Radio Band Sensing (CARABAS) system developed by SAAB AB [65].

Recently, GPR ability to penetrate ice has also triggered the development of satellite-borne radar systems for planetary exploration. For example, SHARAD [66], [67], MARSIS [68], and JAXA's SELENE radar instruments [69] are low-frequency (e.g., few MHz) sounders installed on satellite platforms in orbit around Mars and the moon. The aim of these instruments is to investigate the planet's subsoil. In this regard, an indirect proof of the presence of liquid water on Mars has recently been achieved by processing MARSIS data [70].

DRONE AND UNMANNED AERIAL VEHICLE-BORNE GPRs

An emerging research trend in contactless GPR deals with the exploitation of drones and unmanned aerial vehicles (UAVs). The impetuous development in this field is favored by several factors, such as accurate autonomous flight capability, the possibility of multiple-sensor integration, innovative avionic systems and energy-saving batteries, and a significant reduction of costs and maintenance operations.

The first studies on drone-based radar imaging were reported in [71] and [72]. Later, early tests were carried out by means of UAV-borne radar systems operating at the C [73], P [74], and X [75] bands. Although these high-frequency radars did not allow for significant penetrating capabilities, they did demonstrate the possibility of using imaging radars on UAVs.

The first feasibility study of a multifrequency GPR for rotary UAV platforms was reported in [76] and supported by simulated scenarios. The study aimed at assessing the performance of a GPR operating at 500 MHz and 4 GHz by analyzing the signatures of targets with different sizes and shapes.

An experimental test involving a C-band pulsed radar mounted on a consumer microdrone in DL modality was proposed in [77]. In this work, the imaging performance of the system was assessed by considering the measurement results involving different physical and man-made targets.

Later, a GPR system using two log-periodic dipole array (LPDA) antennas and mounted on a mini-UAV for archaeological prospections was presented in [78]. The system consisted of a light and portable frequency-modulated continuous-wave (FMCW) sensor operating at 745 MHz with 510 MHz of bandwidth. The radar was tested in a controlled environment, showing the ability to detect a buried object at a 0.4-m depth.

A custom-designed, lightweight GPR based on software-defined radio technology mounted on board a minidrone was proposed in [79] for landmine detection. This GPR was lighter than conventional GPR systems and was capable of real-time reconfiguration. As described in [79], the system was able to detect landmines at up to a 0.2-m depth in semiwet terrains (at humidity levels of approximately 70%).

A prototype combining a light and compact radar on-board a commercial minidrone and data processing based on an MWT approach was proposed in [80]. Specifically, the P440 pulsed radar module (Humatics Corporation) operating at 3.95 GHz with 1.7 GHz of bandwidth was employed. A proof-of-concept flight experiment was carried out to assess the imaging capabilities of the prototype and demonstrate the possibility to build up cost-effective UAV-based radar-imaging solutions.

A wideband FMCW GPR operating from 1 up to 4 GHz in a bistatic configuration was presented in [81]. In this case, the radar was designed to balance among weight, size, power consumption, and penetration depth. The system was successfully integrated with horn antennas. A preliminary flight test, with the radar on-board a mini-UAV, demonstrated the system's ability to detect corner reflectors.

Following the encouraging preliminary results, the use of UAV-borne radars has become more attractive in the international scientific community. Recently, an ultra-wideband snow sounder was presented in [82]. The system was designed with a focus on low payload weight to fulfill mini-UAV mounting and high-range resolution requirements for snow measurements. The sensor is a multipurpose microwave device working in the frequency range of 0.1–6 GHz, capable of operating as a microwave imaging system, short-range radar, digital network analyzer, and time-domain reflectometer. In the same context, an analogous drone-borne GPR system was proposed in [83] for soil moisture mapping and precision agriculture applications. The system consists of a handheld vector network analyzer (VNA) working as SFCW radar, and its weight is approximately 1.5 kg. The system is equipped with a lightweight hybrid horn-dipole operating in the 250–2,800-MHz frequency band.

UAVs are equipped with innovative and very accurate positioning strategies for flight trajectories, e.g., by using dual-frequency and multiconstellation GPS receivers combined with differential GPS (DGPS) positioning techniques and inertial measurement units (IMUs). Thanks to these strategies, effective radar data processing techniques have been developed further, improving UAV-based radar-imaging systems. Specifically, [84]–[86] present three different UAV radar-imaging systems based on the use of carrier-based DGPS (CDGPS) to estimate the actual UAV's flight trajectory.

The UAV imaging system in [84], developed by the German Aerospace Center (Deutsches Zentrum für Luft- und Raumfahrt DLR), consisted of a customized version of a DJI Matrice 600pro drone equipped with real-time kinematic (RTK) GPS modules and an IMU for real-time flight-trajectory estimation. An FMCW radar operating in the 500-MHz–3-GHz band, both in slanted synthetic aperture radar imaging and DL-GPR modes, was mounted on the drone.

A system developed at the University of Oviedo [85] exploits a similar version of the DJI Matrice 600pro drone equipped with the same CDGPS-RTK module for UAV remote control. In this case, the radar module was the lightweight and compact P440 pulsed radar module (Humatics Corporation) working in the 3.1–5.1-GHz frequency band, and two customized helix antennas operating with a circular polarization were used. In this way, a tradeoff between range resolution (roughly 7 cm of nominal range resolution) and penetration depth capabilities were achieved.

An improved version of the prototype developed in [80] was presented in [86]. This system exploits the same radar in [80], but the imaging capabilities were improved thanks to the CDGPS positioning technique and novel data processing strategies. The data processing is based on a motion compensation (MoCo) procedure, which exploits the CDGPS positioning to correct the flight quota variations. Moreover, the MWT approach was applied, and its efficient implementation was ensured by adopting a shifting zoom (SZ) approach [62].

It is important to note that one of the main applications of UAV-borne GPR is landmine detection, but the reliable results are mostly concerned with antitank (AT) mines and metallic targets. On the other hand, UAV-based GPR technology is still at an early development stage, and further studies are needed to fully assess its capabilities compared to traditional ground-coupled systems.

GPR DATA PROCESSING

GPR data processing is a very broad research topic as confirmed by the many books and papers that appear in the literature (for example, see [1] and [2] and the references therein). A comprehensive review of these techniques is too long and outside the scope of the present article. A short discussion on the main approaches relevant to contactless GPR is reported as follows.

Here the available data processing techniques are classified as 1) standard processing, 2) imaging/focusing algorithms, 3) full-waveform inversion methods, and 4) machine learning techniques. The first class of procedures aims at filtering clutter and noise, compensating for signal attenuation versus depth, and estimating the wave velocity (permittivity) in the probed medium. This latter information is essential to convert the travel time of the radar echo to a correct depth value. These procedures are exploited in many contactless GPR studies, where the radar data analysis is simply carried out on the basis of a time-/frequency-domain processing of the radargram (B-scan). For instance, this occurs in road inspection by GPR mounted on ground vehicles [19] and in ice exploration via airborne or UAV-borne sounders [49], [50], [57], [58], [61], [76], [79]–[81]. With regard to road inspection, layer thickness is a crucial parameter to be estimated, and its accuracy can be further enhanced by deconvolution techniques [25]. The goal of the deconvolution approach is to recover a sequence of sharp spikes located at the targets' depths starting from a radar trace containing partially overlapping echoes.

The second class of GPR data processing techniques is focusing algorithms [2]. These algorithms take into account that a point-like target appears as a diffraction hyperbola rather than as a point in a GPR image, i.e., the domain defined by the measurement direction and the travel time (range). As shown in the "MWT-Based Signal Processing Strategies" section, focusing/imaging processing is commonly performed after the application of any of the aforementioned time-/frequency-domain operations (e.g., clutter-rejection procedures) as a further processing step devoted to improve the resolution and interpretability of GPR images.

It must be additionally stressed that, in the contactless measurement configuration, the radar signal propagates in air and undergoes a reflection/refraction at the air–soil interface. As result, the scattering model underlying the imaging algorithm has to account for the propagation into an inhomogeneous medium to produce reliable reconstructions of the scene under investigation [2].

A popular imaging approach is migration [87], [88], which is implemented in several commercial tools. Migration can be formulated in the time domain (Kirchhoff migration) or in the ω - k domain (Stolt migration). The latter was originally derived in the seismic context [87] and allows an effective implementation of the focusing by exploiting the Fourier data spectrum. However, this algorithm can be applied only to monostatic radar configurations (e.g., [55] and [56]). Another drawback of migration is its inability to account for severe trajectory motion deviations, thus providing low-accuracy solutions in the case of airborne radar imaging. Nevertheless, migration offers an accurate and efficient solution for spaceborne and ground-based applications.

A similar form of ω - k migration is the diffraction tomographic algorithm (see [2], [89], and [90]). This reconstruction

technique is based on a rigorous solution of the wave equation, and the major approximation involved is the application of the stationary-phase method, which is used to simplify the evaluation of the spectral integral in data modeling. Note that the diffraction tomographic algorithm also assumes a constant antenna height and a flat air–soil interface.

The other forms of migration are reverse-time or diffraction stacking [91], [92], least squares [93], and phase-shift migration [94]. However, these methods have been conceived for ground-coupled GPR.

Other popular imaging approaches are beamforming, matched filtering, and back projection (e.g., see [46], [51], [53], [65], and [85]). These methods are basically equivalent in that they apply a complex weight to the received signals to compensate for the phase delay (shift) produced by a point target. Then, the weighted signals are summed coherently to produce a complex reflectivity map of the scene. A particular implementation of the beamforming technique is the inversion based on the adjoint operator [35]. It must be stressed that beamforming-like algorithms are able to manage MIMO radar configurations [35], [46] and nonrectilinear measurement observation domains [53]. However, their computation complexity is generally higher when compared to migration-like approaches.

Finally, MWT approaches based on the solution of a linear approximation of the EM inverse scattering problem [35], [95], [96] are worth being considered due to their flexibility in dealing with arbitrary measurement configurations (e.g., multibistatic, multiview/multistatic, and so forth), data collection geometries, and background scenarios (e.g., rough terrain profiles). Unlike beamforming, MWT approaches are inverse filtering methods that solve the imaging problem in a more rigorous way by inverting a linear operator. Accordingly, they are generally characterized by enhanced resolution performances than beamforming approaches [97].

The third class of data processing approaches is concerned with full-waveform inversion procedures [98], [99], which are devoted to retrieve quantitative information about the EM properties of the targets by minimizing a cost-functional accounting for “distance” in the data space between the observed and model data. An applicative example regarding contactless GPR is presented in [83], where the quantitative inversion of A-scans collected by a GPR mounted on-board a UAV was carried out with the aim to estimate soil permittivity and subsequently produce spatial maps of water content.

The fourth class of signal processing approaches is based on the use of machine learning or artificial intelligence techniques (e.g., see [100] and the references therein), which have attracted increasing interest in recent years. The main goal of these methods is to solve a very challenging problem: the automatic interpretation of GPR data. Several examples include neural networks (NNs) and support vector machines for automated landmine and UXO detection

[101] or rebar analysis for bridge deck evaluation [102]. More recently, with the rapid development of deep learning [103], convolutional NNs (CNNs) have been proposed for the interpretation of GPR images. CNNs are feature extraction structures characterized by several hidden layers, which can also enhance target detection performance in complex GPR scenarios [104].

CONTACTLESS GPR IMAGING: THE UNIFIED FRAMEWORK OF MWT

FORMULATION OF THE SCATTERING MODEL

The MWT approach formulates the GPR imaging problem as an EM inverse scattering one [2], [18] to retrieve the morphology (location, shape, and size) and EM properties (dielectric permittivity and electrical conductivity) of a buried target, starting from the knowledge of the field backscattered by the target when illuminated by an incident field.

To describe the forward scattering model at the basis of contactless GPR imaging, for the sake of simplicity, we refer to the 2D geometry represented in Figure 1. The scenario features a two-layered medium where the upper half space ($z < 0$) is air while the lower half space ($z > 0$) is soil. The soil medium is assumed to be homogeneous, lossless, non-magnetic, and characterized by the dielectric permittivity ϵ_s . Let D denote the investigation region where the targets are located, and ϵ_t be the unknown target dielectric permittivity. The scene is probed by a couple of Tx and Rx antennas operating in monostatic mode. As shown in Figure 1, the antennas are located at a constant height h above a flat air–soil interface and move along the rectilinear trajectory Γ . The antennas are modeled as electric line sources polarized along the y -axis (transverse magnetic polarization) and work in the angular frequency interval $\Omega = [\omega_{\min}, \omega_{\max}]$. The $\exp(j\omega t)$ time dependence is assumed, where $\omega = 2\pi f$ and

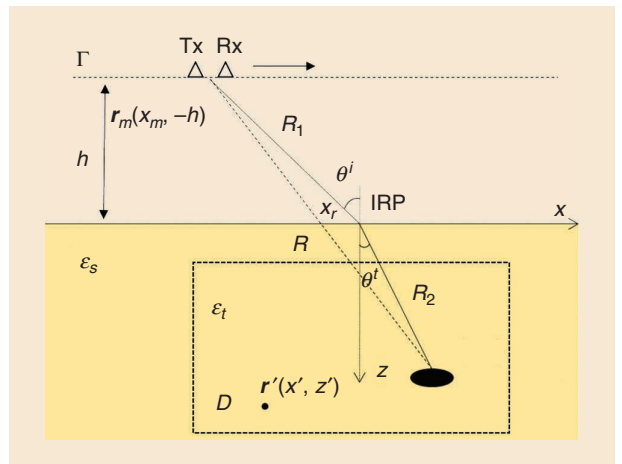


FIGURE 1. A contactless GPR imaging scenario characterized by a two-layered medium, where the upper half space ($z < 0$) is air and the lower half space ($z > 0$) is soil, which is assumed to be homogeneous. The antennas move along a rectilinear path Γ at a constant height h . IRP: interface reflection point.

f is the frequency. The measurement position is denoted by $\mathbf{r}_m(x_m, -h)$, and $\mathbf{r}(x, z)$ is a point in the investigation domain D . The presence of the targets is described by the contrast function $\chi = \epsilon_t/\epsilon_s - 1$, which accounts for the target as an "anomaly" with respect to the EM properties of the soil.

The radar sensing process is governed by the coupled integral equations [105]:

$$E_s(\mathbf{r}_m, \omega) = k_s^2 \iint_D g_e(\mathbf{r}_m, \mathbf{r}, \omega) E_t(\mathbf{r}, \omega) \chi(\mathbf{r}) d\mathbf{r}, \quad (1)$$

$$E_t(\mathbf{r}, \omega) = E_i(\mathbf{r}, \omega) + k_s^2 \iint_D g_i(\mathbf{r}, \mathbf{r}', \omega) E_t(\mathbf{r}', \omega) \chi(\mathbf{r}') d\mathbf{r}', \quad (2)$$

where k_s is the wavenumber in the soil. In the former equations, E_s is the field scattered by the targets (data), and E_t is the total electric field in D , which is equal to the sum of the incident field E_i and an integral accounting for the mutual interactions among targets in D . Moreover, g_e and g_i are the external and internal Green's functions, respectively, of the scenario [105]. The external Green's function g_e expresses the field radiated at \mathbf{r}_m by an elementary source placed at \mathbf{r} . The internal Green's function g_i accounts for the field produced at \mathbf{r} by an elementary source placed at \mathbf{r}' .

The inversion of (1) and (2), i.e., the determination of the contrast function χ from E_s , implies notable mathematical difficulties. Indeed, the problem is nonlinear [2], [18] because E_s is linearly related to the product of E_t and χ [see (1)], but E_t depends on χ through (2). The most important consequence of the nonlinearity is the occurrence of false solutions (local minima) while applying local optimization procedures to minimize a cost function [106], [107]. On the other hand, global optimization procedures, which are known to avoid the local minima problem, imply a notable computational effort, which makes them ill-suited to contactless GPR surveys where large investigation domains are considered, and thus a large number of unknown parameters must be reconstructed. Furthermore, at present, nonlinear inversion methods [18] are not fully suitable for the application in realistic cases due to reliability issues (the presence of false solutions impairing the overall diagnostic procedure) and the effects of model uncertainties and measurement noise.

A notable simplification in the inverse problem is attained by linearizing the scattering equations thanks to the adoption of the Born approximation [105], which neglects the mutual interactions in D [integral in (2)] or equivalently approximate the total field E_t as the incident field E_i . As a result, the data-unknown relationship is given by the linear integral equation:

$$E_s(\mathbf{r}_m, \omega) = k_s^2 \iint_D g_e(\mathbf{r}_m, \mathbf{r}, \omega) E_i(\mathbf{r}, \omega) \chi(\mathbf{r}) d\mathbf{r} = L\chi, \quad (3)$$

where $L: \mathcal{L}^2(D) \rightarrow \mathcal{L}^2(\Gamma \times \Omega)$ is a linear projection operator mapping the unknown space into data space, which is a square-integrable function space.

The linear inverse problem stated by (3) is ill-posed, and this entails that its solution may not exist or that it does not depend continuously on the data [108]. As a result, the presence of noise on the data makes the inversion process unstable, and it is necessary to apply regularization schemes to obtain a solution with a physical meaning. Different regularization strategies can be applied, and here we exploit the truncated singular value decomposition (TSVD) scheme [108]:

$$\tilde{\chi} = \sum_{n=1}^{N_t} \frac{\langle E_s, u_n \rangle}{\sigma_n} v_n, \quad (4)$$

where $\langle \cdot, \cdot \rangle$ is the inner product in data space, $\{\sigma_n, u_n, v_n\}_{n=1}^{\infty}$ is the singular spectrum of the operator L , σ_n are singular values ordered in a descending order, and u_n and v_n are the orthonormal basis functions in the space of data and unknowns, respectively. The regularization parameter N_t is the number of retained singular values, whose value is fixed in such a way as to find a compromise between the resolution and stability of the solution based on the trend of singular values. As discussed in the "Resolution Analysis" section, the necessity to regularize the inverse problem introduces a spatial filtering of the retrievable harmonics of the contrast function (limited spatial resolution), and such filtering is strongly correlated to the adopted measurement configuration [95].

The modulus of the regularized contrast function $\tilde{\chi}$ in (4) defines a spatial map, referred to as a *tomographic image*. This map provides only qualitative information (the position and approximate shape) about the targets.

The linear model in (3) is completely specified once the kernel of the equation, i.e., g_e and E_i , has been made explicit. In the following sections, we review three different models that calculate g_e and E_i by taking into account wave reflection/transmission at the air-soil interface [109].

EVALUATION OF THE GREEN'S FUNCTION AND THE INCIDENT FIELD

SPECTRAL DOMAIN MODEL

An exact expression of g_e and E_i for the half-space scenario in Figure 1 can be achieved by resorting to the plane-wave expansion of the field radiated by an electric line source [105]. Specifically, if the source is located at (x, z) and the measurement point is $(x_m, -h)$, then g_e is written as [2]

$$g_e(x_m, h, x, z, \omega) = \frac{-j}{2\pi} \int_{-\infty}^{\infty} \frac{e^{-jk_{zs}(u)z - jk_{z0}(u)h}}{k_{zs}(u) + k_{z0}(u)} e^{ju(x_m - x)} du, \quad (5)$$

where u is the spectral variable corresponding to the spatial variable x ,

$$k_{z0,s}(u) = \sqrt{k_{0,s}^2 - u^2}, \quad (6)$$

and $k_{0,s}$ denote the wavenumber in free space and in the soil, respectively.

By applying the reciprocity principle [105], the incident field in the soil is expressed in terms of a Green's function as

$$E_i(x, z, x_m, h, \omega) = -j\omega\mu_0 I g_e(x_m, h, x, z, \omega), \quad (7)$$

where I is the electric current amplitude and $\mu_0 = 4\pi \times 10^{-7}$ H/m is the free-space magnetic permeability.

Finally, plugging (5) and (7) into (3) leads to the expression [95]

$$E_s(x_m, h, \omega) = \frac{j\omega\mu_0 I k_s^2}{4\pi^2} \int_{-\infty}^{\infty} \int_{-\infty}^{\infty} \int_{-\infty}^{\infty} e^{j(u+v)x_m} e^{-j(u+v)x} e^{-j(k_{zs}(u) + (k_{zs}(v))z} e^{-j(k_{z0}(u) + k_{z0}(v))h} \times \frac{1}{(k_{zs}(u) + k_{z0}(u))(k_{zs}(v) + k_{z0}(v))} \times \chi(x, z) du dv dz, \quad (8)$$

where v is the spectral variable similar to u .

Note that the model given in (8) does not involve more approximations than the Born approximation. However, (8) involves a noteworthy computational burden because a double-spectral integral needs to be computed for every measurement position x_m , frequency ω , and point (x, z) of the investigation domain to build the operator L . Therefore, the spectral domain (SD) model is not fully suited to process large-scale GPR data and investigation domains.

RAY-BASED MODEL

The quantities g_e and E_i can be evaluated in a simpler way by resorting to a ray-based (RB) modeling of signal propagation [96], which strictly holds under a far-field approximation; i.e., the GPR antennas are far from the investigation domain. According to Figure 1, the signal emitted by the Tx antenna at $(x_m, -h)$ travels along a ray that is transmitted in the soil at the interface reflection point (IRP) x_r and finally reaches the target point (x, z) . The IRP can be determined by applying Snell's law of refraction

$$\sin(\theta^i) = \frac{x_r - x_m}{R_1} = n_s \sin(\theta^t) = n_s \frac{x - x_r}{R_2}, \quad (9)$$

where θ^i and θ^t are the incidence and transmission angles, respectively, with respect to the normal (see Figure 1); $n_s = \sqrt{\epsilon_{rs}}$ is the soil-refractive index (ϵ_{rs} is relative permittivity); and $R_1 = \sqrt{(x_r - x_m)^2 + h^2}$ and $R_2 = \sqrt{(x - x_r)^2 + z^2}$ are the path lengths along the incident and transmitted rays, respectively. Equation (9) leads to a fourth-order polynomial equation with respect to the unknown x_r . The equation can be solved using any nonlinear equation solver by taking into account only the root that fulfills the condition $x_r \leq x$, if $x \geq x_m$ or $x_r \geq x$, if $x \leq x_m$.

Once the IRP is known, g_e and E_i can be straightforwardly calculated by applying geometrical optics concepts, and then the linear integral equation (3) writes as

$$E_s(x_m, h, \omega) = \frac{-jk_s^2 \eta_s I}{8\pi} \iint_D T_{12} T_{21} \frac{e^{-j2k_0(R_1 + n_s R_2)}}{R_1 + R_2} \times \chi(x, z) dx dz, \quad (10)$$

where $\eta_s = \sqrt{\mu_0/\epsilon_s}$ is the soil-intrinsic impedance, and T_{12} and T_{21} are the Fresnel's transmission coefficients at the air-soil interface [110].

The RB model in (10) simplifies the evaluation of the linear operator L with respect to the spectral model in (8). The computation cost for evaluating L is mostly related to the IRP calculation, which involves the solution of a fourth-degree polynomial equation for each pair of measurement and target points.

EQUIVALENT PERMITTIVITY MODEL

To avoid the computational burden of the SD and RB models, an approximated RB model is reported in [109]. This model introduces equivalent permittivity (EP), i.e., an equivalent wavenumber, which allows regarding the propagation in the two-layered scenario as occurring in a medium with an equivalent and spatially varying dielectric permittivity. In other words, an equivalent ray from the source to the target (the dashed line in Figure 1) replaces the actual ray path from the source to the target undergoing refraction at the IRP.

The equivalent wavenumber k_{seq} can be evaluated by matching the phase variation along the ray path in the two-layered medium to the phase in the equivalent medium

$$k_{\text{seq}} R = k_0 (R_1 + n_s R_2), \quad (11)$$

where R is the length of the equivalent-ray path.

In principle, the calculation of k_{seq} in (11) requires computing the IRP for every source and target point as for the RB model. However, the computation can be simplified by assuming a negligible distance between x and x_m , i.e., $x \approx x_m$. Then, (11) writes as

$$k_{\text{seq}} (h + z) = k_0 (h + n_s z), \quad (12)$$

which leads to the relative EP formula

$$\epsilon_{\text{seq}}(z) = \left(\frac{\sqrt{\epsilon_{rs}} z + h}{z + h} \right)^2. \quad (13)$$

The permittivity defined by (13) is equal to the one at the air-soil interface ($z = 0$) and approaches the relative soil permittivity ϵ_{rs} for large z .

According to the EP model, the linear integral equation to be inverted writes as

$$E_s(x_m, h, \omega) = \frac{-jk_s^2 \eta_s I}{8\pi} \iint_D T_{12} T_{21} \frac{e^{-j2k_{\text{seq}} R}}{R} \chi(x, z) dx dz, \quad (14)$$

where the local transmission coefficients T_{12} and T_{21} are evaluated for the ray normal to the air-soil interface.

FREE-SPACE MODEL

A further simplification in the evaluation of g_e and E_i is achieved by resorting to a free-space propagation (FP) model. In particular, when the antenna height is much greater

than the depth of the targets, i.e., $h \gg d$, the propagation in the soil can be considered negligible. This approximation has been adopted in various papers regarding the airborne GPR imaging problem, where shallow targets had to be identified by a radar flying at high altitude [62]. Under this condition, the external Green's function has a very simple analytical form [110]:

$$g_e(x_m, h, x, z, \omega) = \frac{j}{4} H_0^{(2)}(k_0 R), \quad (15)$$

where $H_0^{(2)}$ is the Hankel's function of the second kind and zero order, $R = \sqrt{(x - x_m)^2 + (z + h)^2}$ is the distance between the investigation and measurement points, and $k_0 = \omega/c_0$ ($c_0 = 3e + 8$ m/s is the speed of light in free space).

Upon exploiting the asymptotic approximation of Hankel's function, (15) is rewritten as

$$g_e(x_m, h, x, z, \omega) \approx \frac{1}{2\sqrt{2\pi}k_0} e^{\frac{j3\pi}{4}} \frac{e^{-jk_0 R}}{\sqrt{R}}, \quad (16)$$

and the linear integral equation to be inverted under the FP model is given by

$$E_s(x_m, h, \omega) = \frac{-k_0^2 \eta_0 I}{2\pi} \iint_D \frac{e^{-j2k_0 R}}{R} \chi(x, z) dx dz. \quad (17)$$

RESOLUTION ANALYSIS

Whatever model is adopted to express its kernel, the linear operator L in (3) is compact, and the singular values of its singular spectrum $\{\sigma_n, u_n, v_n\}_{n=1}^\infty$ go to zero as the index n grows up [108]. Therefore, as discussed in the "Formulation of the Scattering Model" section, the inversion process is intrinsically unstable and calls for the adoption of a regularization scheme.

In regard to the TSVD strategy considered in (4), the regularized contrast function is achieved by arresting the summation to the regularization parameter N_t . This implies that the higher-order singular functions associated

with the faster spatial variations of the unknown are filtered, and, hence, only a smoothed version of the contrast (limited resolution) can be reconstructed [2], [95].

A figure of merit used to qualify the spatial harmonics of the regularized contrast function is the spectral content [2], [95]:

$$SC(k_x, k_z) = \sum_{n=1}^{N_t} |\hat{v}_n(k_x, k_z)|^2, \quad (18)$$

where k_x, k_z are the spectral variables corresponding to x, z , respectively, and $\hat{v}_n(k_x, k_z)$ are the 2D Fourier transforms of the singular functions $v_n(x, z)$.

From a more quantitative perspective, the spatial resolution can be estimated in the spatial domain by evaluating the point spread function (PSF), i.e., the regularized reconstruction of a point-like target whose TSVD-based expression writes as

$$\text{PSF}(x, z) = \sum_{n=1}^{N_t} v_n^*(x_0, z_0) v_n(x, z), \quad (19)$$

where (x_0, z_0) is the position of the point target and the symbol $*$ denotes the conjugation operation.

Note that (18) and (19) are powerful mathematical tools that allow for predicting the imaging performance of the linear MWT approach even in unconventional scenarios under arbitrary measurement domains and antenna configurations. Moreover, they can be used to compare the models introduced in the "Evaluation of the Green's Function and the Incident Field" section and thus establish, for the specific case study at hand, the model that ensures the best tradeoff between computational burden and imaging performance in terms of achievable resolution.

An effective analytical representation of the spatial-spectral coverage for the contactless GPR imaging problem in Figure 1 can be found by evaluating, asymptotically, the spectral relationship given in (8). According to [95], under a multimonostatic configuration, the spectral support of the unknown is the annular sector defined by inner and outer radii $2k_{\min}$ and $2k_{\max}$, respectively, and angular coordinates $\pm\theta$ (see Figure 2). In particular, k_{\min} and k_{\max} are the wave-numbers in the soil at the minimum and maximum frequencies, respectively, and θ is the maximum illumination angle ensured by the wave transmitted in the soil. As displayed in Figure 2, the scattering operator acts as a low-pass filter along the horizontal direction and as a bandpass filter along the depth.

With regard to the spatial resolution, simple analytical formulas provide the theoretical limits for contactless multimonostatic GPR configuration [109]:

$$\Delta_x = \frac{c_0}{4f_c \sqrt{\epsilon_{rs}} \sin(\theta)}, \quad (20)$$

$$\Delta_z = \frac{c_0}{2B \sqrt{\epsilon_{rs}}}, \quad (21)$$

where f_c is the central frequency and B is the radar bandwidth.

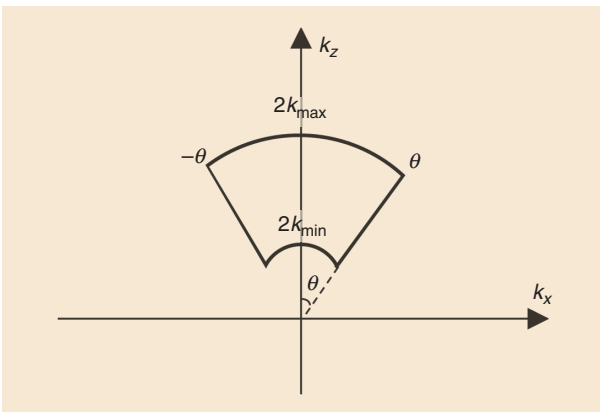


FIGURE 2. The spatial-spectral coverage achieved in a contactless GPR configuration. The annular sector is defined by the inner and outer radii, $2k_{\min}$ and $2k_{\max}$, and the angular coordinates $\pm\theta$. The angle θ is the maximum view angle of the wave transmitted in the soil.

Note that the resolution formulas in (20) and (21) are derived under simplified assumptions (e.g., homogenous soil, rectilinear measurement domains, flat air–soil interfaces, and so on). In more general cases, it is very difficult, if not impossible, to derive closed formulas. Nevertheless, resolution limits can be estimated numerically with the aid of (19).

Note that the spectral contents achieved in single-view/multistatic and multiview/multistatic contactless GPR configurations are derived in a similar way and that their expressions are reported in [95].

CHALLENGES AND PRACTICAL ISSUES

Here we discuss the main technical challenges related to contactless GPR imaging. Note that some of them are common to every GPR application while others are unique to contactless configurations.

CLUTTER

Clutter is a relevant problem affecting the imaging performance of GPR systems [1]. The term *clutter* refers to undesired signal reflections that fall in the measurement time window and interfere with the subsurface targets' features.

Direct coupling between Tx and Rx antennas is the main clutter source for GPR systems. Indeed, when the Tx and Rx antennas are very close to each other or even if a single antenna is used (a monostatic configuration), it is not possible to guarantee a perfect isolation between the Tx and Rx channels. Consequently, a part of the EM signal couples directly from the transmitter into the receiver without interacting with the targets. Direct coupling is an adverse effect because it masks the response of shallow buried targets. A possible way to minimize its effect consists of isolating, as much as possible, the Tx and Rx antennas by placing them in two separate enclosures. This solution also protects the antennas from external interferences (e.g., communication base stations).

In contactless GPRs, direct coupling is no longer a serious problem because it can be distinguished from the surface echo [22] as long as the platform height h is increased. Moreover, in airborne sounding applications where the radar is very far from the ground and high peak power pulses are transmitted, the receiver is turned off during transmission and is activated only after a proper time delay so that the effect of the direct wave is drastically reduced [62].

Nevertheless, direct coupling is usually an unwanted signal to be filtered before the imaging task. To this end, time gating and/or background removal [1] are the most common filtering strategies applied to raw data. These techniques are described later in this article as they are also useful to counteract surface clutter.

Another major clutter source in contactless DL-GPRs is the signal reflection coming from the air–soil interface. This signal may completely obscure the one backscattered by shallower targets, preventing their detection. Ad hoc hardware solutions and data processing methodologies have been proposed to mitigate the reflections from

the air–soil interface. With regard to hardware solutions, it is worth mentioning the differential GPR configuration analyzed in [111]. This configuration directly filters the surface reflection during the survey by recording the difference of the signals at two Rx antennas, which are located at the same height above the air–soil interface and are arranged symmetrically with respect to a central Tx antenna. However, the differential configuration filters out the low-frequency spatial variations of the targets, worsening the imaging quality.

Data processing schemes that filter reflections from the air–soil interface have been proposed [1]. The simplest strategy is time gating, which selects the time interval containing the signals scattered from targets of interest and sets to zero the signal outside such an interval. However, the selection of the optimal time window is a critical issue. Indeed, when the targets are close to the air–soil interface, the time-gating operation may remove a part of the useful signal.

Another popular filtering approach is background removal [2]. This procedure assumes that the clutter response is spatially constant along the measurement direction, i.e., that the air–soil interface is flat. Background removal replaces the current trace (A-scan) with the difference between it and the average value of all the A-scans (or a subset of A-scans close to the trace of interest) in the radargram (B-scan). However, background removal also acts on the signal scattered by the target. As a result, additional compensation procedures are required to restore the PSF [112].

With regard to surface-clutter filtering, the subspace projection method should also be considered [113]. This method assumes that the clutter energy is stronger than the energy backscattered by the target, and, accordingly, its contribution is associated with the highest singular value of the raw data matrix. Therefore, once the SVD of the data matrix has been computed, the gathered data are projected onto the subspace spanned by the singular vectors related to the singular values that are different from the largest ones. A key point of this method is the estimation of the clutter subspace dimension, which is often based on the visual inspection of the curve of the singular values.

Other subspace-based clutter-rejection approaches are principal component and independent component analyses, which are based on matrix decomposition using various constraints in their cost functions [114]. More recently, morphological component analysis [115], nonnegative matrix factorization [116], and robust principal component analysis [117] have also been proposed.

An alternative filtering procedure is the entropy-based time-gating approach [118]. This method performs an automatic selection of the time-gating window on the basis of an entropy criterion. In this way, it is possible to mitigate the clutter contribution due to the air–soil interface as well as the unwanted antenna-ringing effects.

Surface clutter is a common problem in every GPR application; however, it becomes more relevant when radars are mounted on airborne platforms, such as aircraft,

helicopters, and UAVs. Actually, as aircraft fly at high altitudes, the antenna radiation pattern illuminates a wider area on the ground, leading to an increased number of surface returns. Aside from the expected nadir echo, off-nadir returns along and across track are observed. Unfortunately, off-nadir echoes arrive at the radar later than do the nadir echoes; hence, they could be misinterpreted as subsurface reflections (artifacts). The presence of these artifacts becomes noticeable when the observed area is characterized by significant topographic variations, e.g., when monitoring mountain glaciers or desert dunes or, more generally, when man-made structures fall within the antenna footprint [62].

An approach for filtering surface clutter is proposed in [57] with a combined hardware and software strategy. Specifically, the considered radar antenna is a phased array capable of narrowing the beam in the across-track direction, limiting as much as possible the collection of lateral echoes. With regard to the along-track clutter contribution, a zero-Doppler filtering procedure is applied to mitigate its effect. The key idea at the basis of the procedure is that the scattering echoes coming from the off-nadir directions and collected over multiple radar scans are characterized by a Doppler shift with respect to the zero-Doppler nadir echo.

To distinguish the surface echoes from the subsurface ones, an incoherent EM surface scattering simulator was employed for airborne sounding of the Moroccan desert [62]. The simulator takes as input the platform GPS position and the Shuttle Radar Topography Mission digital elevation model of the investigated area to produce a synthetic radar-gram representative of surface-clutter contributions. The comparison between the collected radargram and the synthetic one facilitates the identification of subsurface targets. In the same context, a coherent ray-tracing radar sounder simulator was proposed in [119] to evaluate both surface and subsurface clutter for the regions with an arbitrary number of geological layers. Moreover, an approach used for clutter discrimination that does not require topographic information and that reduces the hardware complexity was proposed in [120]. The approach uses a two-channel sounder and exploits cross-channel interferometric phase differences to differentiate the clutter.

Another clutter source in contactless GPR data is due to ground-surface roughness. Terrain surface is randomly rough and characterized by the presence of objects such as rocks, small plants, bushes, and man-made items. Despite the fact that the waves penetrating the rough terrain are distorted, the main adverse effect is related to the additive clutter noise, which obscures the buried target's response. This phenomenon has been clearly investigated in the framework of landmine detection via FL-GPR systems [35]. Several methods that mitigate the problem have been reported. One solution is that of extracting the target features in order to classify the received signals and separate the target signals from the clutter [121].

Another approach combines the image results obtained by other classes of sensors (e.g., optical sensors) to reduce the false-alarm rate [122], [123]. In [122], an infrared camera, mounted on-board a vehicle, is exploited to estimate the locations of radar clutter sources and eliminate false alarms. In [123], a visible-spectrum color camera is used to retrieve the features related to the target signals. After, the extracted information is exploited in the radar images to discriminate the clutter from the target signatures, thus improving the detection performance. Finally, a real-time 3D modeling of moving-platform FL-GPR scattering from rough terrains located at great electrical distances from the antenna was presented in [43] to mitigate clutter.

MULTIPATH

Multipath effects due to mutual target interactions are additional disturbance sources for GPR imaging. Indeed, the collected radar signal is made up of the direct scattering contributions from targets and multipath contributions, which account for the target-target and target-environment interactions. Many radar-imaging approaches are based on linearized models of the scattering phenomenon, as those in (3). These models account for only direct scattering events and neglect the multipath contributions. Due to this simplified modeling, sometimes reliable imaging results may become difficult to achieve because false targets (ghosts) arise at positions where no real target exists. Therefore, multipath ghost-mitigation procedures are necessary for a correct interpretation of GPR images. The different approaches available in literature are based on subaperture imaging strategies (see, for example, [124] and [125]) or on the exploitation of the nonlinearity of the phase delays experienced by ghosts [126]. In [125], the multipath ghosts' suppression is performed by properly selecting the GPR's measurement setup and applying image-fusion strategies. Specifically, the reconstructions achieved with subarray configurations in the monostatic or single-view/multistatic mode are combined by means of simple arithmetical (additive or multiplicative) image-fusion operations.

The multiplicative subarray image fusion (MSIF) approach has also been compared with the popular coherence factor (CF) filtering technique [127], which mitigates clutter by suppressing its low-coherence features. This comparison has shown that both MSIF and CF are robust with respect to noise and provide similar imaging performance [128]. In addition, MSIF notably improves the imaging quality, yielding less clutter than CF filtering. However, MSIF attenuates the response of the targets as the number of subarrays increases. As a result, MSIF tends to suppress the weaker targets. In conclusion, when a constant false-alarm detection scheme is implemented over the filtered images, both MSIF and CF filtering achieve similar detection performance, so both methods can be successfully exploited to enhance target detectability in highly cluttered environments.

NONRECTILINEAR TRAJECTORIES

A critical point in airborne GPR applications is related to the accurate knowledge of the platform's position during the survey. Indeed, in airborne or UAV-borne GPR imaging, the height of the radar's antenna and the flight's velocity are not constant; in addition, the trajectory, followed by the platform, may deviate significantly from a rectilinear one. As a result, positioning errors, which are comparable to or higher than the operative wavelength, arise, and the radargrams are severely distorted [129]. To avoid this detrimental effect on the radar-imaging's performance, compensation of the deviations with respect to the ideal flight track is a key issue, requiring accurate knowledge of the UAV's platform position and velocity. However, the quality of such information depends on the accuracy of both the embarked navigation sensors and the deployed ground-based tracking devices.

The most popular navigation sensors are IMUs with gyroscopes and accelerometers, magnetometers, and Global Navigation Satellite System (GNSS) receivers (GPS and multiconstellation receivers). The data provided by these devices are typically fused, and the final positioning accuracy is driven by the GNSS receiver, which may reach centimeter-level accuracy. Unfortunately, onboard GPS devices may have performance issues in complex scenarios, such as narrow valleys or near mountains. In these conditions, various solutions can be exploited to correct the motion errors of the platform, such as range finders [130], edge-detection algorithms [80], ground-based tracking devices as robotic total stations [131], and multiple GNSS receivers that enable more sophisticated trajectory reconstruction techniques [86].

An enhanced strategy for reconstructing the UAV's position is based on CDGPS, a recognized technique that enhances positioning accuracy. CDGPS exploits the differences between the measurements collected by two relatively close receivers (one onboard and one ground based) to filter out the common errors affecting them (i.e., satellite clock errors and tropospheric and ionospheric errors). CDGPS data can be generated both in real time or in postprocessing. An RTK CDGPS solution was proposed in [130]. This solution exploits a radio link between a ground receiver and the onboard receiver to perform a real-time control of the flight trajectory with an accuracy of 0.5 cm in the east-north plane and of 1 cm along the vertical direction, thus avoiding artifacts in the image-reconstruction process. A postprocessing kinematic (PPK) CDGPS solution was applied in [86]. The PPK strategy is simpler and less expensive as it does not require any communication link between the GPS receivers. Although it does not allow for real-time control of the airborne trajectory, the PPK technique achieves very accurate offline trajectory estimation, and this information can be used in radar data processing to obtain accurate imaging results.

UAV CHALLENGES

A further key point concerns contactless GPRs mounted on-board a mini- and micro-UAV. This technology offers

several advantages compared to the classic airborne platforms, such as ease of use, flexibility, limited cost, and high survey accuracy. Mini- and micro-UAVs are extremely compact platforms, but they support only a limited payload mass. This entails that a necessary series of tradeoffs have to be sought, concerning the type of components and sensors that can be acquired. For instance, low-weight batteries with limited capacity, compact GPR systems with small and light antennas, and a small number of navigation systems can typically be installed on these platforms. These constraints unavoidably imply a loss in radar penetration capability, reduced autonomy, and a less accurate estimation of the flight's trajectory. Nevertheless, it must be stressed that UAV technology is worth being investigated for its improvements in the coming years.

LARGE-SCALE DATA PROCESSING

Contactless GPR imaging applications require the processing of large-scale (in terms of probing wavelengths) data. In this framework, the inversion of the linear integral equation (3) based on the TSVD regularization scheme is computationally demanding and may become impractical. Accordingly, the SZ approach can be conveniently exploited to reduce the computational effort (see [62] and the references therein).

The SZ approach consists of focusing the data taken from partially overlapping measurement domains and combining the corresponding images in such a way as to get an overall focused image. As schematically represented in Figure 3, the main steps of the SZ procedure are detailed as follows.

- ▶ The measurement line Γ and the surveyed domain D are divided into K partially overlapping subdomains Γ_i and D_i , $i = 1, 2, \dots, K$.
- ▶ For each subdomain D_i , the tomographic reconstruction \tilde{x}_i is obtained by exploiting the TSVD inversion procedure in (4).
- ▶ The tomographic image of the overall surveyed domain D is obtained by combining the K reconstructions \tilde{x}_i achieved for each subdomain D_i .

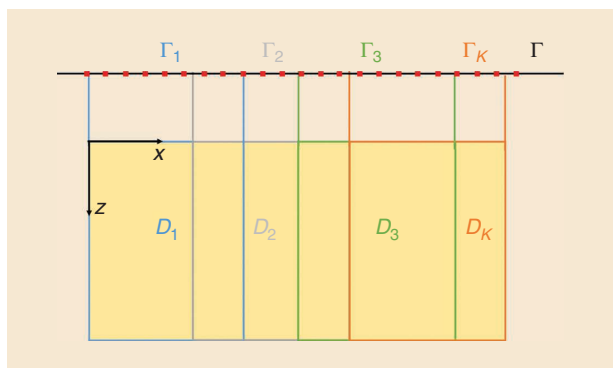


FIGURE 3. The SZ imaging approach. The measurement line Γ and the surveyed domain D are divided into K partially overlapping subdomains.

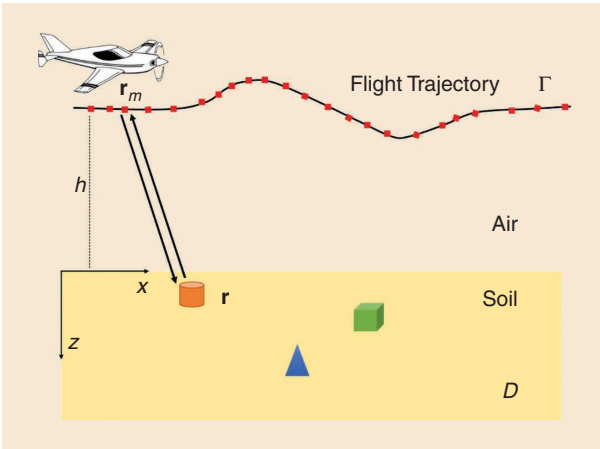


FIGURE 4. An airborne GPR system moves along an arbitrary path Γ , and h denotes a constant reference height. The medium is considered to be homogenous, with buried targets having different shapes and EM properties.

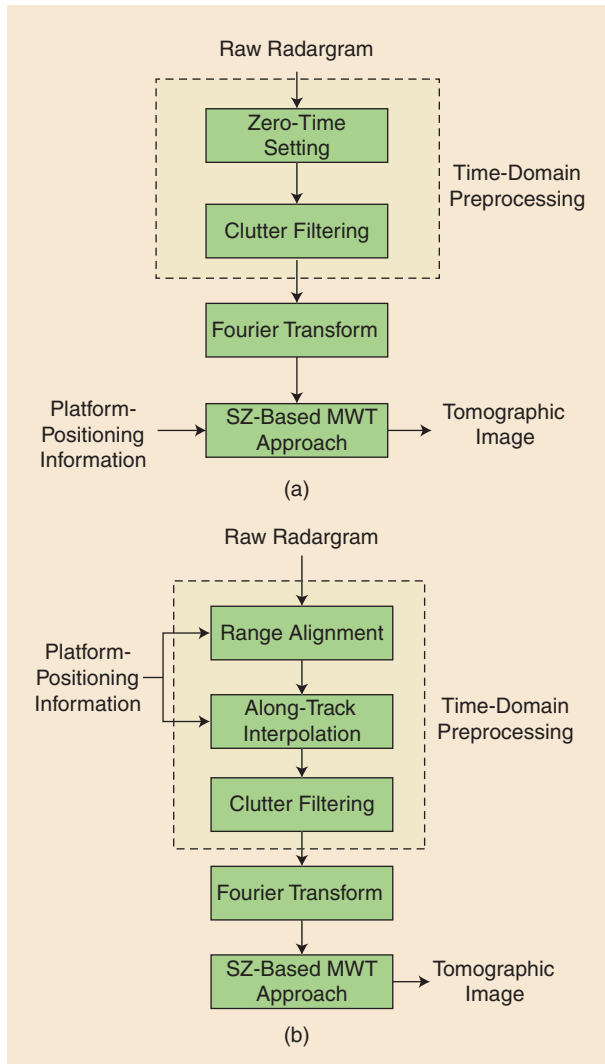


FIGURE 5. The data processing chains for nonrectilinear trajectories. (a) Strategy 1 and (b) strategy 2.

The main benefit offered by the SZ procedure is a computational-effective implementation of the MWT approach. Most notably, if soil permittivity is invariant along the measurement direction, all subdomains D_i have the same size, and the measurement points are evenly spaced and at the same height, the SZ yields a noteworthy reduction of the computational cost required by the computation of the SVD of the scattering operator L in (3).

MWT-BASED SIGNAL PROCESSING STRATEGIES

In this section, we present an overall signal processing procedure based on MWT in the most general case of a nonrectilinear measurement domain (see Figure 4). We recall that this situation arises in the case of flying observation platforms that, different from ground-based vehicles, cannot follow a straight path during radar data acquisition. As is well known, UAVs are affected by wind turbulence and inaccurate piloting commands even when they are controlled by automatic systems or expert pilots. To obtain high-resolution images free from artifacts, it is necessary to retrieve accurate platform positioning information at each measurement point. This information is subsequently exploited to correct the distortions introduced by the nonrectilinear motion of the vehicle. To pursue this goal, two different processing approaches were developed in [62] and [86].

The first one is represented by the block diagram in Figure 5(a) and is referred to as strategy 1. The raw radargram is first processed in the time domain by setting the zero time, i.e., the reference of the two-way travel time axis. After this, the radargram is filtered according to one or more clutter-removal operations previously described in the “Clutter” section. The filtered radargram is transformed in the frequency domain by a Fourier transform operation, and, finally, an SZ-based MWT is implemented based on the TSVD formula in (4). The scattering operator L in (3), to be inverted, accounts for the exact positioning information of the platform provided by onboard navigation sensors [62]. Note that strategy 1 is also suitable for rectilinear trajectories (as it occurs in the case of a ground vehicle).

The second processing strategy (strategy 2) is illustrated in Figure 5(b). This strategy differs from the former one as it implements a MoCo operation directly onto the time-domain data [86]. Specifically, a range alignment of each trace along the nadir direction is carried out to compensate for the altitude variations with respect to a constant reference altitude h (see Figure 4). Then, the along-track interpolation is carried out to account for the along-track velocity variation. Due to the atmospheric turbulence, the along-track velocity cannot be considered constant, thus producing an uneven data sampling along the track. Therefore, the range-aligned radar signals are interpolated and resampled to obtain evenly spaced radar data along the track direction, thus compensating for the velocity variation. The radargram achieved at this stage undergoes a clutter-removal procedure, as described in the “Clutter” section.

Then data are transformed into the frequency domain and inverted according to the SZ-based MWT approach [62].

It must be stressed that the major difference between the strategies is that strategy 1 corrects the motion errors during the focusing stage whereas strategy 2 compensates for them at the data level. Additionally, strategy 2 is more computationally effective because the operator in the SZ-based MWT inversion procedure has to be computed once for every subdomain D_i .

EXPERIMENTAL EXAMPLES

In the following, two examples regarding data collected by means of contactless GPR systems assess the imaging capabilities of the MWT approach. The examples deal with vehicle-based [109] and helicopter-borne [96] GPR imaging.

VEHICLE-BASED GPR IMAGING

Here we present an experimental case study that reproduces, in a simplified way, a demining scenario. This scenario allows for assessing the imaging capabilities of the MWT approach by considering the three models (SD, RB, and EP) in the “Evaluation of the Green’s Function and the Incident Field” section. Specifically, we exploit the data collected during an experiment carried out in 2006 at The Netherlands Organization for Applied Scientific Research (The Hague, The Netherlands). An SFCW radar based on a VNA and horn-antenna collected reflection data in the 800–2,200-band MHz with a step of 6 MHz. The measurement system was mounted on an automated scanner at a height of 0.27 m above a dry sand medium (see Figure 6), which was approximately 3-m deep. The polarization of the illuminating field was in the y direction, and the data were collected along an x -directed profile (see Figure 6).

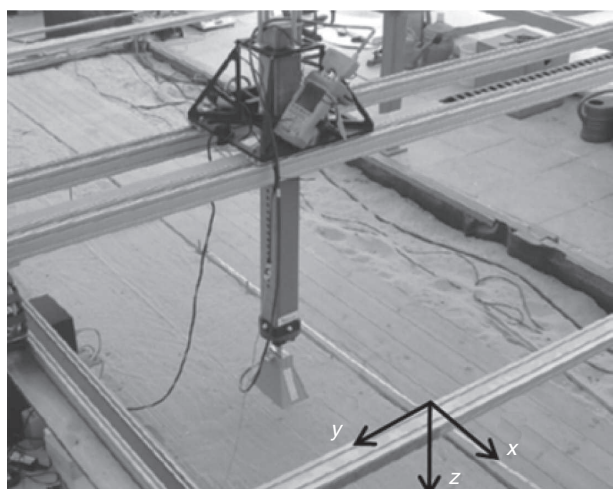


FIGURE 6. A photo of the experimental setup, showing the radar system moved by a linear positioning system [109]. The illuminating field was directed along the y -axis and the data were collected along x -axis.

Three surrogate plastic mines from the Royal Military Academy of Belgium, one AT mine and two antipersonnel mines (PMN2 and M14), were buried in the sand at depths equal to 0.30, 0.12, and 0.10 m, respectively, and positioned over a 2.5-m long profile. For more details regarding the radar system and the setup, the reader is referred to [109] and [132].

Figure 7(a) shows the raw radargram, and its filtered version is in Figure 7(b). The filtered radargram was achieved by applying the clutter-rejection procedure in [109]. The procedure consists of the following three steps. First, the antenna response in the raw data is removed using the far-field radar equation of Lambot et al. [133]. Then, a full-wave inversion is performed by focusing on the surface reflection in the time domain to estimate the sand dielectric permittivity. The retrieved relative permittivity along the survey line varies in the range of 2.68–3.17, with an average value

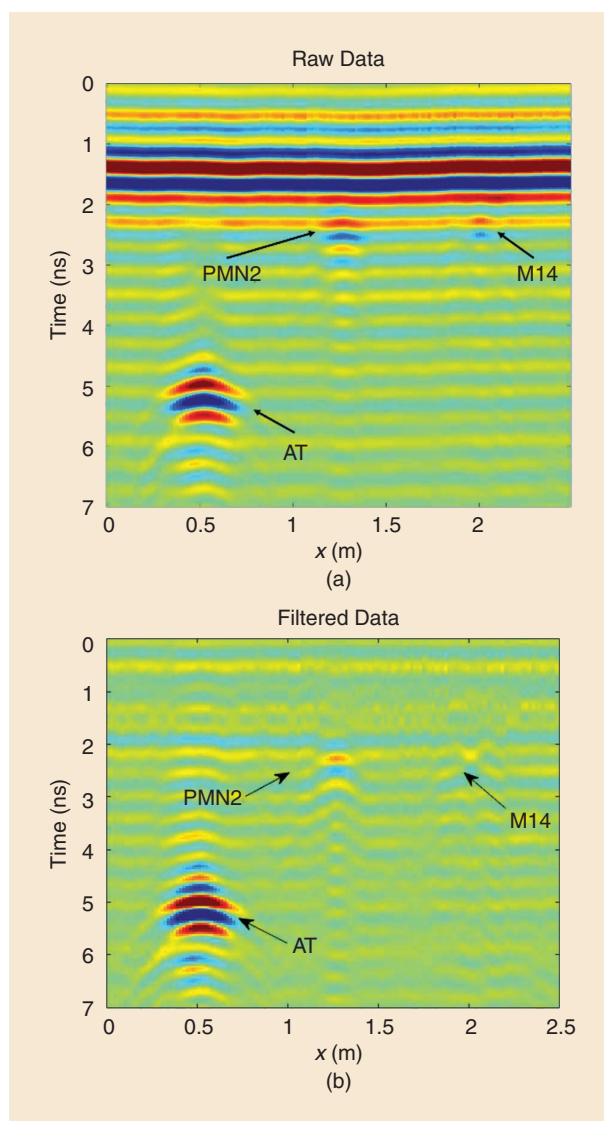


FIGURE 7. (a) A raw radargram. (b) The filtered radargram achieved by applying the clutter-rejection procedure in [109]. The black arrows identify the three plastic mines.

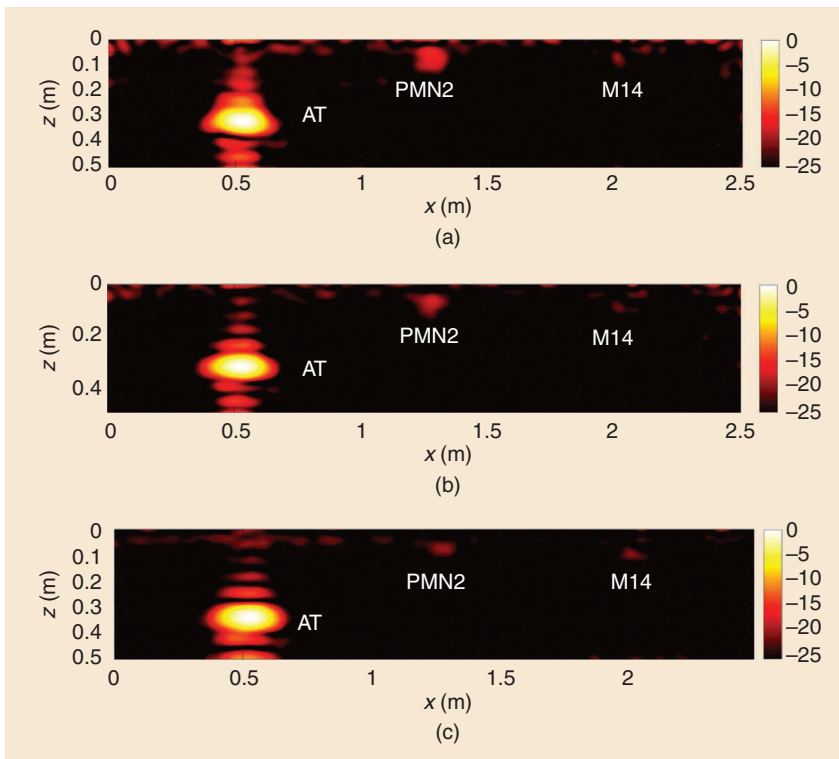


FIGURE 8. The relative amplitude (dB) of the tomographic images. The (a) SD, (b) RB, and (c) EP models.

of roughly 2.9. Based on this permittivity value and exploiting a full-wave radar model, a radargram is simulated for a half-space medium without any target. This synthetic



FIGURE 9. A photo of the gated SFCW helicopter-borne GPR developed by RST GmbH [54]. The system is equipped with two dipole antennas working from 50 to 150 MHz.

radargram is subtracted from the original one to remove the reflection from the air-sand interface [132].

The filtered radargram was transformed into the frequency domain over the 800–2,200-MHz band with a step of 50 MHz, and the sand-relative dielectric permittivity was assumed to be equal to 2.9. Note that, as the sand was dry during the tests, its electrical conductivity was assumed to be negligible. The frequency-domain data were processed in accordance to the MWT approach based on the SD, RB, and EP models, introduced in the “Evaluation of the Green’s Function and the Incident Field” section. The investigation domain $[0, 2.5] \times [0, 0.5]$ m² was considered and discretized into pixels with a size of 0.01 m. The TSVD threshold was set in such way as to neglect the singular values of 20 dB lower than the maximum one.

Figure 8(a)–(c) shows the tomographic images obtained by means of the SD, RB, and EP models, respectively. As can be observed, all of the models allow for detecting the three mines in a reliable way. The stronger response from the AT mine buried at 0.31 m is due to its bigger size (0.25 m along the x -axis) and the higher metal content. Moreover, the presence of some small residual clutter around $z = 0.05$ m is observed due to the clutter-rejection procedure. The best resolution results are achieved by inverting the SD and RB models [see Figure 8(a) and (b)], while the image achieved using the EP model [see Figure 8(c)] is characterized by a slight resolution loss along the x -axis and a small increase of the sidelobes along the z -axis. On the other hand, the loss in terms of resolution of the EP model is compensated for by an improvement of the computational effectiveness compared to the SD and RB models.

The present case has compared three imaging strategies (SD, RB, and EP), whose performances have been improved by an advanced clutter-rejection procedure and assessed by accounting for the data collected in laboratory conditions. The example has also highlighted that the smaller plastic landmine (M14 in Figure 8) provides a weak response, which is difficult to distinguish by the signal, accounting for the reflection from the interface; this means that the response of the M14 target is less detectable compared to the AT and PMN2 targets. This is representative of a general significant issue for landmine detection when the target is shallower (i.e., located at depths of up to 5 cm) because its response can be overwhelmed by the surface echo.

HELICOPTER-BORNE GPR IMAGING

This section presents the results obtained by processing data collected with the helicopter-borne gated SFCW GPR (Figure 9) developed by RST GmbH [54]. The system is equipped with two dipole antennas working from 50 to 150 MHz and uses a reflector to improve directivity and suppress the antenna's back radiation. The system performs 20 frequency sweeps per second with 512 programmable frequency steps.

The data set was collected on the Grenzgletscher glacier, an alpine-temperate glacier located in the Zermatt region, Switzerland. The investigated glacier is known to have many crevasses, which made impossible the execution of in situ surveys [54].

The radar data were collected along a nearly 6-km-long flight track, with an average spacing of 1.02 m between the scans, and the position of the platform was recorded by the onboard GPS. The radargram achieved by performing an inverse Fourier transform of the frequency domain raw data is depicted in Figure 10 as a function of the travel time and the distance along the track. The radargram reveals several interesting features. In particular, it is possible to identify an area characterized by cold ice (the central portion of the radargram), where the volumetric scattering is limited, and the regions made by temperate ice (the left and right sides of the radargram), where strong scattering occurs. In the cold ice region, various localized anomalies appear, and the bottom of the glacier is also clearly identified at travel times around 4,000 ns.

The portion of the radargram in Figure 10 corresponding to the interval from 1,700 to 4,180 m was processed according to strategy 2, as described in Figure 5(b). First, the variations of the flight height of the helicopter were corrected along the range based on the altitude information provided by the GPS. Then, a time gating was applied up to 900 ns to reject the direct antenna coupling and the signal reflections

from the glacier surface. The obtained radargram is plotted in Figure 11(a), where the travel time has been converted to the depth from the surface by assuming an ice-relative dielectric permittivity equal to 3 [134].

The filtered radargram, presented in Figure 11(a), was then transformed into the frequency domain, and these data were inverted by applying the SZ-based MWT approach. The data window length in the SZ approach was chosen equal to 100 m, and the local investigation domain $[0, 1] \times [50], [350]$ m² was discretized with a spatial step of 0.5 m. Note that the linear integral equation to be inverted was fixed on the basis of the EP model [see (14)]. The TSVD threshold for the inversion was set in such a way as to filter the singular values lower than 20 dB with respect to the maximum one.

The achieved tomographic image is displayed in Figure 11(b). As observed, the image is better resolved compared to the radargram. The localized anomalies seen as diffraction hyperbolas in Figure 11(a) [see also Figure 11(c)] are represented as well-focused spots [see Figure 11(d)]. Among them, the scatterers located at a distance of 1,840 m and extending to a depth range from 80 to 150 m may be crevasses or large rocks. Finally, the bedrock of the glacier located at variable depths in the range from 280 to 330 m in Figure 11(b) is also better emphasized by the focusing procedure.

The described case study validated strategy 2 in a realistic and challenging scenario. By modeling radar signal propagation through an air-ice interface and compensating for the variation of the flight's height, it is possible to focus raw data correctly and detect buried localized anomalies.

CONCLUSIONS

This article addressed the challenges and related solution strategies for a reliable and effective subsurface imaging via contactless GPR. The problems share some common points with the classical ground-coupled GPR, but, at the same

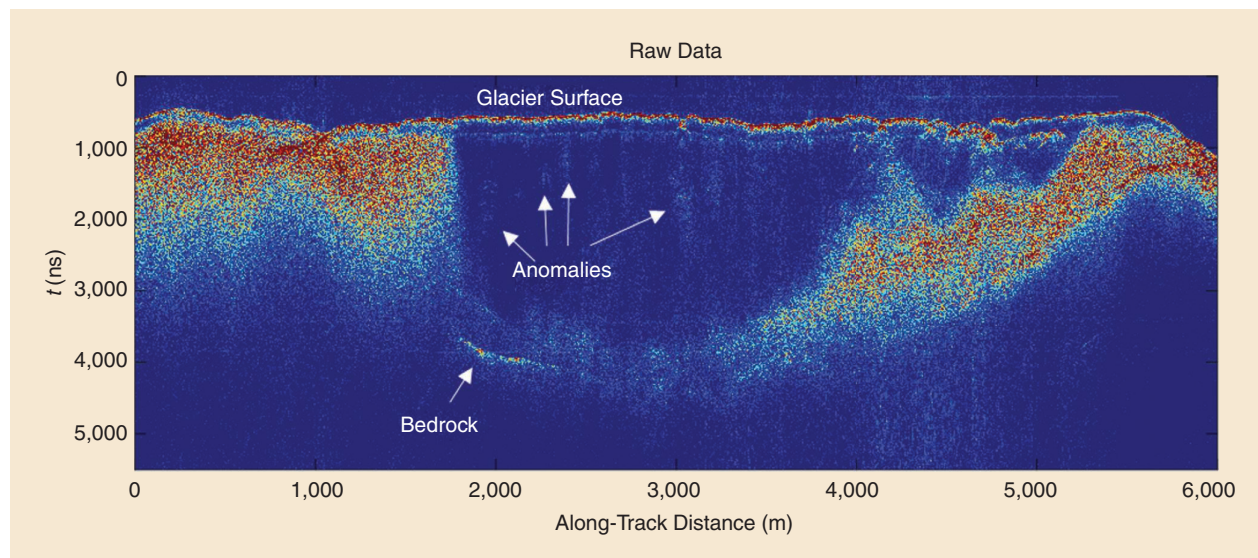


FIGURE 10. A radargram of the GPR survey performed over the Grenzgletscher glacier. The color scale is [0.01 0.1].

time, further difficulties arise because the radar antenna is far from the air–soil interface.

On one side, the massive amount of collected data calls for computationally efficient data processing strategies, which should be able to account for a reference scenario that cannot be easily schematized as a homogeneous medium. In the contactless configuration, the EM wave propagates in a stratified medium made by air and the medium hosting the targets; therefore, the wave-refraction phenomenon has to be taken into account to perform reliable imaging. In this respect, few models have been presented to balance between the computation effectiveness of the solution approach (pushing toward approximate EM propagation models) and the imaging accuracy in terms of the localization and geometry estimation of the buried targets. Note that nonlinear (quantitative) imaging methods have

limited applicability for large-scale surveys because they exhibit reliability issues, demand a huge computation effort, and are not fully robust with respect to the model's uncertainties and noise.

Apart from EM modeling aspects, further issues arise when GPR is allocated on airborne/UAV platforms. These issues are related to the increasing clutter amount and deviations of the flight's trajectory with respect to the "ideal" one (i.e., rectilinear trajectory at a constant height). With respect to this second issue, two different strategies based on the linear MWT approach have been presented to mitigate the problem. The first one exploits the exact measurement points directly in the inverse model. The second one is based on a MoCo procedure, which corrects the motion-induced distortions in the data; thus, the inversion algorithms valid under the rectilinear trajectory assumption can be applied.

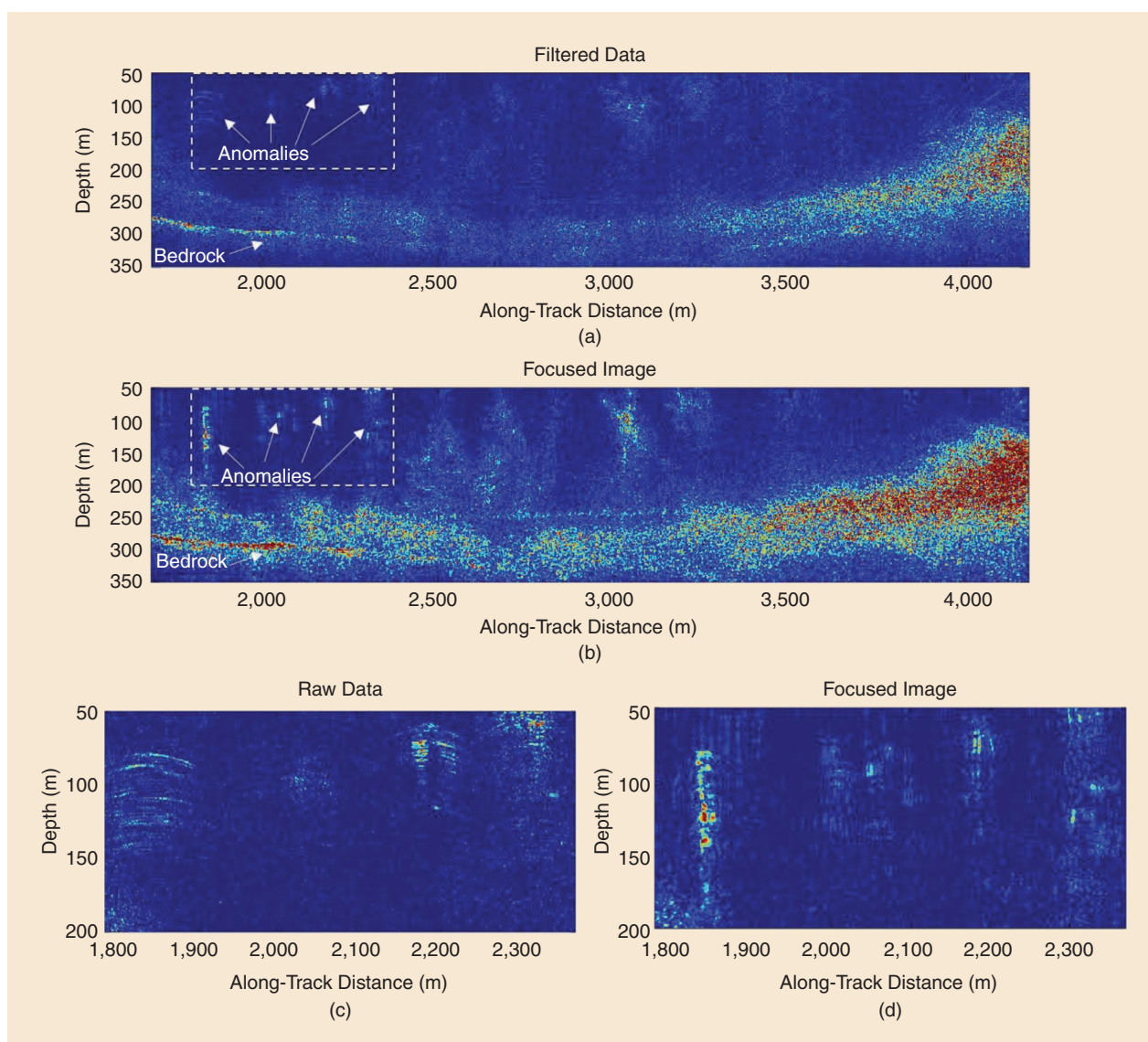


FIGURE 11. (a) A zoom image of the radargram over the interval from 1,700 to 4,180 m and at a depth range from 50 to 350 m. (b) A focused image. (c) A zoom image of the radargram and (d) a focused image over the interval from 1,780 to 2,370 m and at a depth range from 40 to 200 m. The color scale is [0.01 0.1].

An issue worth being investigated in the future is related to the information content of the backscattered field data. Such an amount of information is limited because in contactless GPR the antennas are often several wavelengths away from the investigated region, and the domain is “viewed” under an angle that becomes smaller as the height of the observational platforms increases. Therefore, it is necessary to assess the performance of the inversion algorithm in terms of the resolution and spatial variability of the unknown object function. This investigation is also important to determine the measurement configuration parameters (e.g., the spatial and frequency steps), ensuring a nonredundant data acquisition. A few studies have been made in 2D cases, but a research effort is necessary to address 3D cases.

Future developments must address the extension of the presented 2D approaches to the case of full 3D imaging. This requires advances in data processing and, most notably, in nonredundant data collection strategies. Finally, the possibility of real-time onboard data processing calls for the development of completely automated data processing strategies able to perform an effective and robust imaging.

ACKNOWLEDGMENTS

All the authors contributed equally to the preparation of the article.

AUTHOR INFORMATION

Ilaria Catapano (catapano.i@irea.cnr.it) is with the Institute for Electromagnetic Sensing of the Environment, National Research Council of Italy, I-80124, Italy.

Gianluca Gennarelli (gennarelli.g@irea.cnr.it) is with the Institute for Electromagnetic Sensing of the Environment, National Research Council of Italy, Naples, I-80124, Italy.

Giovanni Ludeno (ludeno.g@irea.cnr.it) is with the Institute for Electromagnetic Sensing of the Environment, National Research Council of Italy, Naples, I-80124, Italy.

Carlo Noviello (noviello.c@irea.cnr.it) is with the Institute for Electromagnetic Sensing of the Environment, National Research Council of Italy, Naples, I-80124, Italy.

Giuseppe Esposito (esposito.g@irea.cnr.it) is with the Institute for Electromagnetic Sensing of the Environment, National Research Council of Italy, Naples, I-80124, Italy.

Francesco Soldovieri (soldovieri.f@irea.cnr.it) is with the Institute for Electromagnetic Sensing of the Environment, National Research Council of Italy, Naples, I-80124, Italy.

REFERENCES

- [1] D. J. Daniels, *Ground Penetrating Radar*. Hoboken, NJ: Wiley, 2005.
- [2] R. Persico, *Introduction to Ground Penetrating Radar: Inverse Scattering and Data Processing*. Hoboken, NJ: Wiley, 2014.
- [3] I. Catapano, G. Gennarelli, G. Ludeno, F. Soldovieri, and R. Persico, “Ground-penetrating radar: Operation principle and data processing,” in *Wiley Encyclopedia of Electrical and Electronics Engineering*. Hoboken, NJ: Wiley, 2019, pp. 1–23.
- [4] S. A. Arcone, “High resolution of glacial ice stratigraphy: a ground-penetrating radar study of Pegasus Runway, McMurdo Station, Antarctica,” *Geophysics*, vol. 61, no. 6, pp. 1653–1663, 1996. doi: 10.1190/1.1444084.
- [5] J. L. Davis and A. P. Annan, “Ground-penetrating radar for high-resolution mapping of soil and rock stratigraphy,” *Geophys. Prospect.*, vol. 37, no. 5, pp. 531–551, 1989. doi: 10.1111/j.1365-2478.1989.tb02221.x.
- [6] A. P. Annan, “GPR methods for hydrogeological studies,” *Hydrogeophysics*. Dordrecht: Springer-Verlag, 2005.
- [7] A. Benedetto, “Water content evaluation in unsaturated soil using GPR signal analysis in the frequency domain,” *J. Appl. Geophys.*, vol. 71, no. 1, pp. 26–35, 2010. doi: 10.1016/j.jappgeo.2010.03.001.
- [8] J. L. Porsani, W. A. Sauck, and A. O. S. Júnior, “GPR for mapping fractures and as a guide for the extraction of ornamental granite from a quarry: A case study from southern Brazil,” *J. Appl. Geophys.*, vol. 58, no. 3, pp. 177–187, 2006. doi: 10.1016/j.jappgeo.2005.05.010.
- [9] D. Goodman and S. Piro, *GPR Remote Sensing in Archaeology*. New York: Springer, 2013.
- [10] I. Trinks et al., “Large-area high-resolution ground-penetrating radar measurements for archaeological prospection,” *Archaeol. Prospection*, vol. 25, no. 3, pp. 171–195, 2018. doi: 10.1002/arp.1599.
- [11] A. M. Alani, M. Aboutalebi, and G. Kilic, “Applications of ground penetrating radar (GPR) in bridge deck monitoring and assessment,” *J. Appl. Geophys.*, vol. 97, pp. 45–54, Oct. 2013. doi: 10.1016/j.jappgeo.2013.04.009.
- [12] A. Benedetto and L. Pajewski, *Civil Engineering Applications of Ground Penetrating Radar*. London: Springer-Verlag, 2015.
- [13] A. Novo, H. Lorenzo, F. I. Rial, and M. Solla, “3D GPR in forensics: finding a clandestine grave in a mountainous environment,” *Forensic Sci. Int.*, vol. 204, nos. 1–3, pp. 134–138, 2011. doi: 10.1016/j.forsciint.2010.05.019.
- [14] D. J. Daniels, “A review of GPR for landmine detection,” *Sens. Imag.*, vol. 7, no. 3, p. 90, 2006. doi: 10.1007/s11220-006-0024-5.
- [15] M. Lazzari, A. Loperte, and A. Perrone, “Near surface geophysics techniques and geomorphological approach to reconstruct the hazard cave map in historical and urban areas,” *Adv. Geosci.*, vol. 24, pp. 35–44, Mar. 2010. doi: 10.5194/adgeo-24-35-2010.
- [16] X. Long et al., “A young multilayered terrane of the northern Mare Imbrium revealed by Chang'E-3 mission,” *Science*, vol. 347, no. 6227, pp. 1226–1229, 2015. doi: 10.1126/science.1259866.
- [17] M. El Said, “Geophysical prospection of underground water in the desert by means of electromagnetic interference fringes,” *Proc. IRE*, vol. 44, no. 1, pp. 24–30, 1956. doi: 10.1109/JRPROC.1956.274846.
- [18] M. Pastorino, *Microwave Imaging*. Hoboken, NJ: Wiley, 2010.
- [19] A. Benedetto, F. Tosti, L. Bianchini Ciampoli, and F. D’Amico, “An overview of ground-penetrating radar signal processing techniques for road inspections,” *Signal Process.*, vol. 132, pp. 201–209, Mar. 2017. doi: 10.1016/j.sigpro.2016.05.016.
- [20] W. Shao, A. Bouzerdoum, S. L. Phung, L. Su, B. Indraratna, and C. Rujikiatkamjorn, “Automatic classification of ground-penetrating-radar signals for railway-ballast assessment,” *IEEE*

- Trans. Geosci. Remote Sens.*, vol. 49, no. 10, pp. 3961–3972, 2011. doi: 10.1109/TGRS.2011.2128328.
- [21] X. L. Travassos, S. L. Avila, R. L. d. S. Adriano, and N. Ida, "A review of ground penetrating radar antenna design and optimization," *J. Microw., Optoelectron. Electromagn. Appl.*, vol. 17, no. 3, pp. 385–402, 2018. doi: 10.1590/2179-10742018v17i31321.
 - [22] N. Diamanti and A. P. Annan, "Air-launched and ground-coupled GPR data," in *Proc. 11th Eur. Conf. Antennas Propag. (EuCAP)*, Paris, 2017, pp. 1694–1698. doi: 10.23919/EuCAP.2017.7928409.
 - [23] T. Saarenketo and T. Scullion, "Road evaluation with ground penetrating radar," *J. Appl. Geophys.*, vol. 43, nos. 2–4, pp. 119–138, 2000. doi: 10.1016/S0926-9851(99)00052-X.
 - [24] J. Hugenschmidt, "Concrete bridge inspection with a mobile GPR system," *Construction Building Mater.*, vol. 16, no. 3, pp. 147–154, 2002. doi: 10.1016/S0950-0618(02)00015-6.
 - [25] I. L. Al-Qadi and S. Lahouar, "Measuring layer thicknesses with GPR—Theory to practice," *Construction Building Mater.*, vol. 19, no. 10, pp. 763–772, 2005. doi: 10.1016/j.conbuildmat.2005.06.005.
 - [26] D. H. Chen, F. Hong, W. Zhou, and P. Ying, "Estimating the hotmix asphalt air voids from ground penetrating radar," *NDT E Int.*, vol. 68, pp. 120–127, Dec. 2014. doi: 10.1016/j.ndteint.2014.08.008.
 - [27] K. Hoegh, L. Khazanovich, S. Dai, and T. Yu, "Evaluating asphalt concrete air void variation via GPR antenna array data," *Case Stud. Nondestructive Testing Eval.*, vol. 3, pp. 27–33, Apr. 2015. doi: 10.1016/j.cnsdt.2015.03.002.
 - [28] J. Hugenschmidt, "Railway track inspection using GPR," *J. Appl. Geophys.*, vol. 43, nos. 2–4, pp. 147–155, 2000. doi: 10.1016/S0926-9851(99)00054-3.
 - [29] W. Al-Nuaimy, A. Eriksen, and J. Gasgoyne, "Train-mounted GPR for high-speed rail trackbed inspection," in *Proc. 10th Int. Conf. Ground Penetrating Radar*, Delft, The Netherlands, 2004, pp. 631–634.
 - [30] F. Benedetto, F. Tosti, and A. M. Alani, "An entropy-based analysis of GPR data for the assessment of railway ballast conditions," *IEEE Trans. Geosci. Remote Sens.*, vol. 55, no. 7, pp. 3900–3908, 2017. doi: 10.1109/TGRS.2017.2683507.
 - [31] L. Bianchini Ciampoli, A. Calvi, and F. D'Amico, "Railway ballast monitoring by GPR: A test-site investigation," *Remote Sens.*, vol. 11, no. 20, pp. 2381, 2019. doi: 10.3390/rs11202381.
 - [32] Y. Zan, Z. Li, G. Su, and X. Zhang, "An innovative vehicle-mounted GPR technique for fast and efficient monitoring of tunnel lining structural conditions," *Case Stud. Nondestructive Testing Eval.*, vol. 6, pp. 63–69, Nov. 2016. doi: 10.1016/j.cnsdt.2016.10.001.
 - [33] J. Kositsky, R. Cosgrove, C. Amazeen, and P. Milanfar, "Results from a forward-looking GPR mine detection system," in *Proc. SPIE*, 2002, vol. 4742, pp. 206–217.
 - [34] T. Jin, J. Lou, and Z. Zhou, "Extraction of landmine features using a forward-looking ground-penetrating radar with MIMO array," *IEEE Trans. Geosci. Remote Sens.*, vol. 50, no. 10, pp. 4135–4144, 2012. doi: 10.1109/TGRS.2012.2188803.
 - [35] F. Soldovieri, G. Gennarelli, I. Catapano, D. Liao, and T. Dogaru, "Forward-looking radar imaging: a comparison of two data processing strategies," *IEEE J. Sel. Topics Appl. Earth Observ. Remote Sens.*, vol. 10, no. 2, pp. 562–571, 2017. doi: 10.1109/JSTARS.2016.2543840.
 - [36] J. A. Camilo, L. M. Collins, and J. M. Malof, "A large comparison of feature-based approaches for buried target classification in forward-looking ground-penetrating radar," *IEEE Trans. Geosci. Rem. Sens.*, vol. 56, no. 1, pp. 547–558, 2018. doi: 10.1109/TGRS.2017.2751461.
 - [37] D. Liao, T. Dogaru, and A. Sullivan, "Large-scale, full-wave-based emulation of step-frequency forward-looking radar imaging in rough terrain environments," *Sens. Imag. Int. J. (Springer)*, vol. 15, no. 1, pp. 1–29, 2014.
 - [38] E. M. Rosen, F. S. Rotondo, and A. Elizabeth, "Testing and evaluation of forward-looking GPR countermeasure systems," in *Proc. SPIE*, 2005, vol. 5794, pp. 901–911. doi: 10.1117/12.603734.
 - [39] X. Zhuge, A. G. Yarovoy, T. Savelyev, and L. Ligthart, "Modified Kirchhoff migration for UWB MIMO array-based radar imaging," *IEEE Trans. Geosci. Remote Sens.*, vol. 48, no. 6, pp. 2692–2703, 2010. doi: 10.1109/TGRS.2010.2040747.
 - [40] Y. Wang, X. Li, Y. Sun, J. Li, and P. Stoica, "Adaptive imaging for forward-looking ground penetrating radar," *IEEE Trans. Aerosp. Electron. Syst.*, vol. 41, no. 3, pp. 922–936, July 2005. doi: 10.1109/TAES.2005.1541439.
 - [41] M. Ressler, L. Nguyen, F. Koenig, D. Wong, and G. Smith, "The Army Research Laboratory (ARL) synchronous impulse reconstruction (SIRE) forward-looking radar," in *Proc. SPIE*, 2007, vol. 6561, pp. 656–105. doi: 10.1117/12.719688.
 - [42] D. W. Paglieroni, D. H. Chambers, J. E. Mast, S. W. Bond, and N. R. Beer, "Imaging modes for ground penetrating radar and their relation to detection performance," *IEEE J. Sel. Topics Appl. Earth Observ. Remote Sens.*, vol. 8, no. 3, pp. 1132–1144, 2014. doi: 10.1109/JSTARS.2014.2357718.
 - [43] M. M. Tajdini, B. Gonzalez-Valdes, J. A. Martinez-Lorenzo, A. W. Morgenthaler, and C. M. Rappaport, "Real-time modeling of forward-looking synthetic aperture ground penetrating radar scattering from rough terrain," *IEEE Trans. Geosci. Remote Sens.*, vol. 57, no. 5, pp. 2754–2765, 2018. doi: 10.1109/TGRS.2018.2876808.
 - [44] D. Comite, F. Ahmad, M. G. Amin, and T. Dogaru, "Forward-looking ground-penetrating radar: Subsurface target imaging and detection: A review," *IEEE Geosci. Remote Sens. Mag.*, early access, Feb. 2021. doi: 10.1109/MGRS.2020.3048368.
 - [45] A. D. Pambudi, M. Fauß, F. Ahmad, and A. M. Zoubir, "Mini-max robust landmine detection using forward-looking ground-penetrating radar," *IEEE Trans. Geosci. Remote Sens.*, vol. 58, no. 7, pp. 5032–5041, 2020. doi: 10.1109/TGRS.2020.2971956.
 - [46] D. Comite, F. Ahmad, T. Dogaru, and M. Amin, "Coherence-factor-based rough surface clutter suppression for forward-looking GPR imaging," *Remote Sens.*, vol. 12, no. 5, p. 857, 2020. doi: 10.3390/rs12050857.
 - [47] J. C. Cook, "Proposed monocycle-pulse very-high-frequency radar for airborne ice and snow measurement," *AIEE*

- Commun. Electron.*, vol. 79, no. 5, pp. 588–594, 1960. doi: 10.1109/TCE.1960.6367316.
- [48] J. Bailey, S. Evans, and G. d Q. Robin, "Radio echo sounding of polar ice sheets," *Nature*, vol. 204, no. 4957, pp. 420–421, 1964. doi: 10.1038/204420a0.
 - [49] S. M. Hodge, D. L. Wright, J. A. Bradley, R. W. Jacobel, N. Skou, and B. Vaughn, "Determination of the surface and bed topography in central Greenland," *J. Glaciol.*, vol. 36, no. 122, pp. 17–30, 1990. doi: 10.3189/S0022143000005505.
 - [50] S. Gogineni, T. Chuah, C. Allen, K. Jezek, and R. K. Moore, "An improved coherent radar depth sounder," *J. Glaciol.*, vol. 44, no. 148, pp. 659–669, 1998. doi: 10.3189/S0022143000002161.
 - [51] J. Li et al., "High-altitude radar measurements of ice thickness over the Antarctic and Greenland ice sheets as a part of operation icebridge," *IEEE Trans. Geosci. Remote Sens.*, vol. 51, no. 2, pp. 742–754, Feb. 2013. doi: 10.1109/TGRS.2012.2203822.
 - [52] F. Rodriguez-Morales et al., "Advanced multifrequency radar instrumentation for polar research," *IEEE Trans. Geosci. Remote Sens.*, vol. 52, no. 5, pp. 2824–2842, 2013. doi: 10.1109/TGRS.2013.2266415.
 - [53] F. Hélière, C. Lin, H. Corr, and D. Vaughan, "Radio echo sounding of Pine Island Glacier, West Antarctica: Aperture synthesis processing and analysis of feasibility from space," *IEEE Trans. Geosci. Remote Sens.*, vol. 45, no. 8, pp. 2573–2582, 2007. doi: 10.1109/TGRS.2007.897433.
 - [54] D. Eisenburger, H. Lentz, and M. Jenett, "Helicopter-borne GPR systems: A way from ice thickness measurements to geological applications," in *Proc. IEEE Int. Conf. Ultra-Wideband*, 2008, pp. 161–165. doi: 10.1109/ICUWB.2008.4653441.
 - [55] E. Rignot, J. Mouginot, C. F. Larsen, Y. Gim, and D. Kirchner, "Low-frequency radar sounding of temperate ice masses in Southern Alaska," *Geophys. Res. Lett.*, vol. 40, no. 20, pp. 5399–5405, 2013. doi: 10.1002/2013GL057452.
 - [56] J. Mouginot, E. Rignot, Y. Gim, D. Kirchner, and F. Le Meur, "Low-frequency radar sounding of ice in East Antarctica and southern Greenland," *Ann. Glaciol.*, vol. 55, no. 67, pp. 138–146, 2014. doi: 10.3189/2014AoG67A089.
 - [57] D. J. Kristensen, S. S. Krozer, V. Hernández, C. C. Vidkjær, J. Kusk, and E. L. Christensen, "ESA's polarimetric airborne radar ice sounder (POLARIS): Design and first results," *IET Radar Sonar Navigation*, vol. 4, no. 3, pp. 488–496, 2010. doi: 10.1049/iet-rsn.2009.0035.
 - [58] M. J. Øyan, S. E. Hamran, L. Damsgård, and T. Berger, "Compact airborne C-Band radar sounder," *IEEE Trans. Geosci. Remote Sens.*, vol. 52, no. 10, pp. 6326–6332, 2014. doi: 10.1109/TGRS.2013.2296074.
 - [59] E. Nilot et al., "Design and performance of full-polarimetric airborne GPR testing system," *Proc. 15th Int. Conf. Ground Penetrating Radar (GPR)*, 2014, pp. 807–810. doi: 10.1109/ICGPR.2014.6970537.
 - [60] J. H. Bradford, D. F. Dickins, and P. J. Brandvik, "Assessing the potential to detect oil spills in and under snow using airborne ground-penetrating radar," *Geophysics*, vol. 75, no. 2, pp. G1–G12, 2010. doi: 10.1190/1.3312184.
 - [61] E. Heggy, P. A. Rosen, R. Beatty, T. Freeman and Y. Gim, "Orbiting Arid Subsurface and Ice Sheet Sounder (OASIS): Exploring desert aquifers and polar ice sheets and their role in current and paleo-climate evolution," in *Proc. IEEE Int. Geosci. Remote Sens. Symp. - IGARSS*, Melbourne, VIC, 2013, pp. 3483–3486. doi: 10.1109/IGARSS.2013.6723579.
 - [62] G. Gennarelli, P. A. Rosen, R. Beatty, T. Freeman, and Y. Gim, "A low frequency airborne GPR system for wide area geophysical surveys: The case study of Morocco Desert," *Remote Sens. Environ.*, vol. 233, p. 111409, Nov. 2019. doi: 10.1016/j.rse.2019.111409.
 - [63] R. Firoozabadi, E. L. Miller, C. M. Rappaport, and A. W. Morgenthaler, "Subsurface sensing of buried objects under a randomly rough surface using scattered electromagnetic field data," *IEEE Trans. Geosci. Remote Sens.*, vol. 45, no. 1, pp. 104–117, 2007. doi: 10.1109/TGRS.2006.883462.
 - [64] M. E. Davis, *Foliage Penetration Radar – Detection and Characterization of Objects Under Trees*. Raleigh, NC: SciTech Publishing, Apr. 2011.
 - [65] H. Hellsten, S. Sahlin, and P. Dammert, "Polarimetric subsurface SAR imaging outcome of theoretical development and CARABAS III tests," in *Proc. Int. Radar Conf.*, Lille, France, 2014, pp. 1–8. doi: 10.1109/RADAR.2014.7060256.
 - [66] R. Seu et al., "SHARAD: The MRO 2005 shallow radar," *Planetary Space Sci.*, vol. 52, nos. 1–3, pp. 157–166, 2004. doi: 10.1016/j.pss.2003.08.024.
 - [67] R. Croci, R. Seu, E. Flamini, and E. Russo, "The SHallow RADAR (SHARAD) onboard the NASA MRO mission," *Proc. IEEE*, vol. 99, no. 5, pp. 794–807, 2011. doi: 10.1109/JPROC.2010.2104130.
 - [68] G. Picardi et al., "Radar soundings of the subsurface of Mars," *Science*, vol. 310, no. 5756, pp. 1925–1928, 2005. doi: 10.1126/science.1122165.
 - [69] T. Ono et al., "Lunar radar sounder observations of subsurface layers under the nearside maria of the Moon," *Science*, vol. 323, no. 5916, pp. 909–912, 2009. doi: 10.1126/science.1165988.
 - [70] R. Orosei et al., "Radar evidence of sub-glacial liquid water on Mars," *Science*, vol. 361, no. 6401, pp. 490–493, 2018. doi: 10.1126/science.aar7268.
 - [71] R. Giret, H. Jeuland, and P. Enert, "A study of a 3D-SAR concept for a millimeter wave imaging radar onboard an UAV," in *Proc. 1st Eur. Radar Conf.*, 2004, pp. 201–204.
 - [72] M. Weiss and J. H. G. Ender, "A 3D imaging radar for small unmanned airplanes-ARTINO," in *Proc. Eur. Radar Conf.*, 2005, pp. 209–212. doi: 10.1109/EURAD.2005.1605602.
 - [73] E. Zaugg et al., "Using the microASAR on the NASA SIERRA UAS in the characterization of Arctic sea ice experiment," in *Proc. IEEE Radar Conf.*, 2010, pp. 271–276. doi: 10.1109/RADAR.2010.5494611.
 - [74] M. A. Remy, K. AC de Macedo, and J. R. Moreira, "The first UAV-based P-and X-band interferometric SAR system," *Proc. IEEE Int. Geosci. Remote Sens. Symp.*, 2012, pp. 5041–5044. doi: 10.1109/IGARSS.2012.6352478.
 - [75] A. Aguasca, R. Acevo-Herrera, A. Broquetas, J. J. Mallorqui, and X. Fabregas, "ARBRES: Light-weight CW/FM SAR sensors for small UAVs," *Sensors*, vol. 13, no. 3, pp. 3204–3216, 2013. doi: 10.3390/s130303204.
 - [76] A. Amiri, K. Tong, and K. Chetty, "Feasibility study of multi-frequency Ground Penetrating Radar for rotary UAV platforms," in *Proc. IET Int. Conf. Radar Syst.*, 2012.

- [77] C. J. Li and H. Ling, "High-resolution, downward-looking radar imaging using a small consumer drone," in *Proc. IEEE Int. Symp. Antennas Propag. (APSURSI)*, 2016, pp. 2037–2038. doi: 10.1109/APS.2016.7696725.
- [78] M. A. Yarlequ , S. Alvarez, and H. J. Mart nez. "FMCW GPR radar mounted in a mini-UAV for archaeological applications: First analytical and measurement results," in *Proc. Int. Conf. Electromagn. Adv. Appl. (ICEAA)*, 2017, pp. 1646–1648. doi: 10.1109/ICEAA.2017.8065606.
- [79] J. Colorado et al., "An integrated aerial system for landmine detection: SDR-based Ground Penetrating Radar onboard an autonomous drone," *Adv. Robot.*, vol. 31, no. 15, pp. 791–808, 2017. doi: 10.1080/01691864.2017.1351393.
- [80] G. Ludeno, I. Catapano, A. Renga, A. R. Vetrella, G. Fasano, and F. Soldovieri, "Assessment of a micro-UAV system for micro-wave tomography radar imaging," *Remote Sens. Environ.*, vol. 212, pp. 90–102, June 2018. doi: 10.1016/j.rse.2018.04.040.
- [81] R. Burr, M. Schartely, P. Schmidt, W. Mayerz, T. Walter, and C. Waldschmidt, "Design and implementation of a FMCW GPR for UAV-based mine detection," in *Proc. IEEE MTT-S Int. Conf. Microw. Intell. Mobility*, 2018, pp. 1–4. doi: 10.1109/ICMIM.2018.8443526.
- [82] R. O. R. Jenssen, M. Eckerstorfer, and S. Jacobsen, "Drone-mounted ultrawideband radar for retrieval of snowpack properties," *IEEE Trans. Instrum. Meas.*, vol. 69, no. 1, pp. 221–230, 2019. doi: 10.1109/TIM.2019.2893043.
- [83] K. Wu et al., "A new drone-borne GPR for soil moisture mapping," *Remote Sens. Environ.*, vol. 235, p. 111456, Dec. 2019. doi: 10.1016/j.rse.2019.111456.
- [84] S. Dill, E. Schreiber, M. Engel, A. Heinzl, and M. Peichl, "A drone carried multichannel Synthetic Aperture Radar for advanced buried object detection," in *Proc. IEEE Radar Conf.*, 2019, pp. 1–6. doi: 10.1109/RADAR.2019.8835814.
- [85] M. G. Fern ndez et al., "Synthetic aperture radar imaging system for landmine detection using a ground penetrating radar onboard an unmanned aerial vehicle," *IEEE Access*, vol. 6, pp. 45,100–45,112, Aug. 2018.
- [86] C. Noviello, G. Esposito, G. Fasano, A. Renga, F. Soldovieri, and I. Catapano, "Small-UAV radar imaging system performance with GPS and CDGPS based motion compensation," *Remote Sens.*, vol. 12, no. 20, p. 3463, 2020. doi: 10.3390/rs12203463.
- [87] R. H. Stolt, "Migration by Fourier transform," *Geophysics*, vol. 43, no. 1, pp. 23–48, 1978. doi: 10.1190/1.1440826.
- [88] X. Feng and M. Sato, "Pre-stack migration applied to GPR for landmine detection," *Inverse Problems*, vol. 20, no. 6, p. S99, 2004. doi: 10.1088/0266-5611/20/6/S07.
- [89] A. J. Devaney, "Geophysical diffraction tomography," *IEEE Trans. Geosci. Remote Sens.*, vol. GE-22, no. 1, pp. 3–13, 1984. doi: 10.1109/TGRS.1984.350573.
- [90] L. Qu, Z. Liu, and Y. Sun, "Diffraction tomographic imaging algorithm for airborne ground penetrating radar," in *Proc. 15th Int. Conf. Ground Penetrating Radar*, 2014, pp. 659–662. doi: 10.1109/ICGPR.2014.6970508.
- [91] E. Baysal, D. D. Kosloff, and J. W. Sherwood, "Reverse time migration," *Geophysics*, vol. 48, no. 11, pp. 1514–1524, 1983. doi: 10.1190/1.1441434.
- [92] G. T. Schuster, "Reverse-time migration - generalized diffraction stack migration," in *Proc. SEG Tech. Program Expanded Abstracts*, 2002, pp. 1280–1283. doi: 10.1190/1.1816888.
- [93] T. Nemeth, C. Wu, and G. T. Schuster, "Least-squares migration of incomplete reflection data," *Geophysics*, vol. 64, no. 1, pp. 208–221, 1999. doi: 10.1190/1.1444517.
- [94] J. Gazdag, "Wave equation migration with the phase-shift method," *Geophysics*, vol. 43, no. 7, pp. 1342–1351, 1978. doi: 10.1190/1.1440899.
- [95] R. Persico, "On the role of measurement configuration in contactless GPR data processing by means of linear inverse scattering," *IEEE Trans. Geosci. Remote Sens.*, vol. 54, no. 7, pp. 2062–2071, 2006. doi: 10.1109/TAP.2006.877170.
- [96] I. Catapano, L. Crocco, Y. Krellmann, G. Trilitzsch, and F. Soldovieri, "Tomographic airborne ground penetrating radar imaging: achievable spatial resolution and on-field assessment," *ISPRS J. Photogram. Remote Sens.*, vol. 92, pp. 69–78, June 2014. doi: 10.1016/j.isprsjprs.2014.01.011.
- [97] I. Catapano, F. Soldovieri, G. Alli, G. Mollo, and L. A. Forte, "On the reconstruction capabilities of beamforming and a microwave tomographic approach," *IEEE Geosci. Remote Sens. Lett.*, vol. 12, no. 12, pp. 2369–2373, 2015. doi: 10.1109/LGRS.2015.2476514.
- [98] G. Meles, S. Greenhalgh, J. Van der Kruk, A. Green, and H. Maurer, "Taming the non-linearity problem in GPR full-waveform inversion for high contrast media," *J. Appl. Geophys.*, vol. 78, pp. 31–43, Mar. 2012. doi: 10.1016/j.jappgeo.2011.12.001.
- [99] S. Busch, J. van der Kruk, J. Bikowski, and H. Vereecken, "Quantitative conductivity and permittivity estimation using full-waveform inversion of on-ground GPR data," *Geophysics*, vol. 77, no. 6, pp. H79–H91, 2012. doi: 10.1190/geo2012-0045.1.
- [100] X. L. Travassos, S. L. Avila, and N. Ida, "Artificial neural networks and machine learning techniques applied to ground penetrating radar: A review," *Appl. Comput. Inf.*, vol. 17, no. 2, pp. 296–308, 2020. doi: 10.1016/j.aci.2018.10.001.
- [101] X. Nunez-Nieto, M. Solla, P. Gomez-Perez, and H. Lorenzo, "GPR signal characterization for automated landmine and UXO detection based on machine learning techniques," *Remote Sens.*, vol. 6, no. 10, pp. 9729–9748, 2014. doi: 10.3390/rs6109729.
- [102] P. Kaur, K. J. Dana, F. A. Romero, and N. Gucunski, "Automated GPR rebar analysis for robotic bridge deck evaluation," *IEEE Trans. Cybern.*, vol. 46, no. 10, pp. 2265–2276, 2015. doi: 10.1109/TCYB.2015.2474747.
- [103] Y. LeCun, Y. Bengio, and G. Hinton, "Deep learning," *Nature*, vol. 521, no. 7553, pp. 436–444, 2015. doi: 10.1038/nature14539.
- [104] Z. Tong, J. Gao, and D. Yuan, "Advances of deep learning applications in ground-penetrating radar: A survey," *Construction Building Mater.*, vol. 258, p. 120,371, Oct. 2020. doi: 10.1016/j.conbuildmat.2020.120371.
- [105] W. C. Chew, *Waves and Fields in Inhomogeneous Media*. Piscataway, NJ: Institute of Electrical and Electronics Engineers, 1995.
- [106] T. Isernia, V. Pascazio, and R. Pierri, "On the local minima in a tomographic imaging technique," *IEEE Trans. Geosci. Remote Sens.*, vol. 39, no. 7, pp. 1596–1607, 2001. doi: 10.1109/36.934091.
- [107] M. Ambrosanio, M. T. Bevacqua, T. Isernia, and V. Pascazio, "Performance analysis of tomographic methods against

- experimental contactless multistatic ground penetrating radar," *IEEE J. Sel. Topics Appl. Earth Observ. Remote Sens.*, vol. 14, pp. 1171–1183, 2021. doi: 10.1109/JSTARS.2020.3034996.
- [108] M. Bertero and P. Boccacci, *Introduction to Inverse Problems in Imaging*. Bristol: Institute of Physics Publishing, 1998.
- [109] G. Ludeno, G. Gennarelli, S. Lambot, F. Soldovieri, and I. Catapano, "A comparison of linear inverse scattering models for contactless GPR imaging," *IEEE Trans. Geosci. Remote Sens.*, vol. 58, no. 10, pp. 7305–7316, 2020. doi: 10.1109/TGRS.2020.2981884.
- [110] C. A. Balanis, *Advanced Engineering Electromagnetics*. New York: Wiley, 2012.
- [111] R. Persico and F. Soldovieri, "A microwave tomography approach for a differential configuration in GPR prospecting," *IEEE Trans. Antennas Propag.*, vol. 54, no. 11, pp. 3541–3548, 2006. doi: 10.1109/TAP.2006.882161.
- [112] R. Persico and F. Soldovieri, "Effects of background removal in linear inverse scattering," *IEEE Trans. Geosci. Remote Sens.*, vol. 46, no. 4, pp. 1104–1114, 2008. doi: 10.1109/TGRS.2007.910223.
- [113] M. Garcia-Fernandez et al., "SVD-based clutter removal technique for GPR," in *Proc. IEEE Int. Symp. Antennas Propagation & U.S. Nat. Committee/Int. Union Radio Science Nat. Radio Science Meeting*, 2017, pp. 2369–2370. doi: 10.1109/APUSNCURSINRSM.2017.8073227.
- [114] P. K. Verma, A. N. Gaikwad, D. Singh, and M. J. Nigam, "Analysis of clutter reduction techniques for through wall imaging in UWB range," *Prog. Electromagn. Res.*, vol. 17, pp. 29–48, Aug. 2009. doi: 10.2528/PIERB09060903.
- [115] E. Temlioglu and I. Erer, "Clutter removal in ground-penetrating radar images using morphological component analysis," *IEEE Geosci. Remote Sens. Lett.*, vol. 13, no. 12, pp. 1802–1806, 2016. doi: 10.1109/LGRS.2016.2612582.
- [116] D. Kumlu and I. Erer, "Clutter removal in GPR images using non-negative matrix factorization," *J. Electromagn. Waves Appl.*, vol. 32, no. 16, pp. 2055–2066, 2018. doi: 10.1080/09205071.2018.1489740.
- [117] X. Song, D. Xiang, K. Zhou, and Y. Su, "Improving RPCA-based clutter suppression in GPR detection of antipersonnel mines," *IEEE Geosci. Remote Sens. Lett.*, vol. 14, no. 8, pp. 1338–1342, 2017. doi: 10.1109/LGRS.2017.2711251.
- [118] R. Solimene, A. Cuccaro, A. Dell'Aversano, I. Catapano, and F. Soldovieri, "Ground clutter removal in GPR surveys," *IEEE J. Sel. Topics Appl. Earth Observ. Remote Sens.*, vol. 7, no. 3, pp. 792–798, 2014. doi: 10.1109/JSTARS.2013.2287016.
- [119] C. Gerekos, A. Tamponi, L. Carrer, D. Castelletti, M. Santoni, and L. Bruzzzone, "A coherent multilayer simulator of radar-grams acquired by radar sounder instruments," *IEEE Trans. Geosci. Remote Sens.*, vol. 56, no. 12, pp. 7388–7404, 2018. doi: 10.1109/TGRS.2018.2851020.
- [120] D. Castelletti et al., "An interferometric approach to cross-track clutter detection in two-channel VHF radar sounders," *IEEE Trans. Geosci. Remote Sens.*, vol. 55, no. 11, pp. 6128–6140, 2017. doi: 10.1109/TGRS.2017.2721433.
- [121] T. Wang, J. M. Keller, P. D. Gader, and O. Sjahputera, "Frequency subband processing and feature analysis of forward-looking ground penetrating radar signals for land-mine detection," *IEEE Trans. Geosci. Remote Sens.*, vol. 45, no. 3, pp. 718–729, 2007. doi: 10.1109/TGRS.2006.888142.
- [122] K. Stone, J. Keller, K. Ho, M. Busch, and P. Gader, "On the registration of FLGPR and IR data for a forward-looking landmine detection system and its use in eliminating FLGPR false alarms," in *Proc. Defense, Security Sens. Symp. Int. Society Optics Photonics*, Orlando, FL, Apr. 2008, p. 695,314.
- [123] T. C. Havens et al., "Improved detection and false alarm rejection using FLGPR and color imagery in a forward-looking system," in *Proc. SPIE, Detection Sensing Mines, Explosive Objects, Obscured Targets XV*, Apr. 2010, vol. 7664. doi: 10.1117/12.852274.
- [124] D. Obuchon, D. Garren, J. S. Goldstein, R. Greene, and J. North, "Drift inversion estimation of multipath ghosts in SAR image reconstruction," in *Proc. IEEE Radar Conf.*, 2004, pp. 556–558. doi: 10.1109/NRC.2004.1316486.
- [125] G. Gennarelli and F. Soldovieri, "Multipath ghosts in radar imaging: Physical insight and mitigation strategies," *IEEE J. Sel. Topics Appl. Earth Observ. Remote Sens.*, vol. 8, no. 3, pp. 1078–1086, 2015. doi: 10.1109/JSTARS.2014.2363233.
- [126] J. DeLaurentis, "Multipath synthetic aperture radar imaging," *IET Radar, Sonar Navig.*, vol. 5, no. 5, pp. 561–572, 2011. doi: 10.1049/iet-rsn.2010.0225.
- [127] R. J. Burkholder and K. E. Browne, "Coherence factor enhancement of through-wall radar images," *IEEE Antennas Wireless Propag. Lett.*, vol. 9, pp. 842–845, Aug. 2010. doi: 10.1109/LAWP.2010.2069078.
- [128] G. Gennarelli, G. Vivone, P. Braca, F. Soldovieri, and M. G. Amin, "Comparative analysis of two approaches for multipath ghost suppression in radar imaging," *IEEE Geosci. Remote Sens. Lett.*, vol. 13, no. 9, pp. 1226–1230, 2016. doi: 10.1109/LGRS.2016.2577715.
- [129] M. Soumekh, *Synthetic Aperture Radar Signal Processing*, vol. 7. New York: Wiley, 1999.
- [130] M. Garcia-Fernandez, Y. Alvarez-Lopez, and F. Las Heras, "Autonomous airborne 3D SAR imaging system for subsurface sensing: UWB-GPR onboard a UAV for landmine and IED detection," *Remote Sens.*, vol. 11, no. 20, p. 2357, 2019. doi: 10.3390/rs11202357.
- [131] H. Chao, Y. Gu, and M. Napolitano, "A survey of optical flow techniques for robotics navigation applications," *J. Intell. Robot. Syst.*, vol. 73, nos. 1–4, pp. 361–372, 2013. doi: 10.1007/s10846-013-9923-6.
- [132] O. Lopera, E. C. Slob, N. Milisavljevic, and S. Lambot, "Filtering soil surface and antenna effects from GPR data to enhance landmine detection," *IEEE Trans. Geosci. Remote Sens.*, vol. 45, no. 3, pp. 707–717, 2007. doi: 10.1109/TGRS.2006.888136.
- [133] S. Lambot, E. C. Slob, I. van den Bosch, B. Stockbroeckx, and M. Vanclooster, "Modeling of ground-penetrating radar for accurate characterization of subsurface electric properties," *IEEE Trans. Geosci. Remote Sens.*, vol. 42, no. 11, pp. 2555–2568, 2004. doi: 10.1109/TGRS.2004.834800.
- [134] S. Evans, "Dielectric properties of ice and snow—a review," *J. Glaciol.*, vol. 5, no. 42, pp. 773–792, 1965. doi: 10.3189/S0022143000018840.